Doctoral Thesis

Development of the atomic and electronic structure analysis method for the hetero interface of semiconductor devices

Nara Institute of Science and Technology

Graduate School of Materials Science

Surface and Materials Science Laboratory

Naoyuki Maejima

(Thesis supervisor Prof. Hiroshi Daimon)

March 17, 2014

Contents

Chapter 1

Introduction

1.1 Background

Various electronic devices make our modern life convenient. Many people started to use smartphone and tablet in 2013 in Japan. Up to now, most thin film transistors (TFT) for displays in smartphones and tablets have been made by silicon(Si) semiconductor. The high performance products of it were expansion of demand. However Si TFT cannot achieve high resolution display due to its limit of device performance which was predicted from Si electron mobility. Thus, high resolution display was achieved by Indium gallium zinc oxide (InGaZnO) TFT. The big earthquake hit the whole Tohoku area in 2011. The nuclear power plants were stopped because of some troubles and inspection. The government requested the energy saving to the public. Wide bandgap semiconductor is promissing material for power devices. 10% saving energy of electronic car comparing to Si devices was achieved with SiC power devices. In such a way, the performance of Si device become reaching the limits. Therefore, new materials realizing higher

performance devices were required. The atomic structure of hetero interface betweem semiconductor and insulator is important for device character, because the defect states at the interface such as dangling bond are caused by non-ideal atomic configuration. Investigation of the character of new material for making electronic devices became difficult because the electronic devices has become nano scale. Intel co. sold new Central Processing Unit(CPU) which included 22 nm-gate-length Metal-oxide-semiconductor(MOS) devices in 2013. Thus, sub nano meter scale characterization method which means "atomic structure analysis of semiconductor" is necessary. Thus, we developed atomic level semiconductor characterization methods for investigation of new materials.

1.2 Atomic level semiconductor characterization methods

The transmission electron microscopy(TEM) is one of the most conventional atomic structure analysis method. This observation method requires to slice the sample to several tens nano meter thickness. The observation result is an average along to sample thickness direction. Thus, the local atomic structure around each atom site cannot be observed by TEM.

The atomic resolution is achieved by scanning tunneling microscope(STM). How-

ever, it can observe only the electronic structure at the topmost surface of sample. We have to break the sample to observe the interface of hetero structure.
In such way, we have to break the sample when we use these conventional methods to observe buried interface atomic structure. However, the interface atomic structure might be changed by this breaking process. Thus, we need nondestructive atomic structure observation method.

1.3 Photoelectron diffraction spectroscopy

Photoelectron diffraction is a powerful element-selective atomic structure analysis method, which has direct access to buried subsurfaces and interfaces without destroying surfaces. C.S Fadley reported emission angle dependence of photoelectron from single crystal metal in 1971[1] . Liebsch started theoretical study of photoelectron diffraction in 1974[2]. After that, many researchers used photoelectron diffraction to investigate adsorbate on surface.[3, 4, 5] The Si and Ge hetero interface structure was investigated by photoelectron diffraction in 1989.[7] After that, an oxide and Si and SiC interface was investigated by photoelectron diffraction.[8, 9]

Site-specific X-ray photoelectron spectroscopy (XPS) and XAS can be obtained by analyzing forward focusing peaks (FFPs) and diffraction patterns as site specific probes. For example, the electronic and magnetic structures of each atomic layer

of a Ni thin film was investigated using atomic layer specific FFPs for resolving site-specific XAS spectra.[10, 11] In an previous work[12], we measured Si 2p and C 1s PIADs from the vicinal 6H-SiC(0001) substrate with an epitaxial SiON thin film. There are two different Si and C sites in SiC crystals owing to stacking faults. Owing to the anisotropic step bunching along the [11$\bar{2}$0] direction resulting in a preferential appearance of terraces with one type of local atomic site,[29] threefold symmetric photoelectron intensity angular distributions (PIADs) predominantly originating from top layers were obtained. We developed a numerical method of deducing PIAD from each site by solving an inverse matrix.

1.4 Problems about SiC devices and previous works

The development of power devices is an urgent contemporary issue. Silicon carbide (SiC) is a key material for finding such a solution owing to its wide band gap, high break down field, and high electron mobility.[13] Furthermore, thermal silicon oxide layers can be grown on SiC, which is common to Si surfaces. Accordingly, processing techniques in the Si industry is applied to SiC device fabrications. In reality, the conventional oxide films have a few nm-thick transition layer at the interface, which seriously affects the transport property.[14] An epitaxial silicon

oxide layer with an atomically sharp interface was reported.[15] However, the epitaxial silicon oxide layer on SiC(0001) has a dangling bond per unit cell at the interface.[15, 9] This problem is expected to be solved by nitrogen incorporation leading to the formation of an epitaxial oxynitride (SiON) layer that completely lifts the interfacial dangling bond. [16] Nitrogen atom, which have one valence electron more than the oxygen atom, removes the interface defect state.

Shirasawa *et al.* have reported an investigation of a new stable epitaxial SiON thin film on 6H-SiC(0001) [17] by scanning tunneling microscopy and low energy electron diffraction (LEED) I-V measurements. They suggested an atomic structure model of the epitaxial SiON thin film on SiC(0001) that consist of Si_2O_5 thin film, a Si_2N_3 layer at the interface, and a SiC substrate. In addition, in the Si_2O_5 thin film, tridymite- and cristobalite-like 180° Si-O-Si bonds coexist with quartz-like 144° Si-O-Si bonds. The dangling-bond free interface was achieved in their model. Recently, vertical atomic layer distances have been confirmed by X-ray diffraction.[18]

It is essential to characterize local electronic structures to understand the origin of the epitaxial SiON thin-film stability. The atomically abrupt band offset at the interface of SiON/SiC(0001) was confirmed by X-ray absorption spectroscopy (XAS) and X-ray emission spectroscopy (XES) together with theoretical calculation.[19] XAS measurements were performed in the total electron yield

(TEY) and Auger electron yield (AEY) detection modes. AEY detection was expected to be more surface sensitive than TEY detection due to the finite mean escape depth of Auger electron. Two kinds of oxygen atoms were placed at sites of different depth in the oxide layer. However, the surface sensitivity difference in XAS by the AEY and TEY detection modes was not sufficient to resolve the electronic structure for two different oxygen sites then. I investigated aluminum nitride thin film on non-polar SiC in Chapter 3. Group-III nitride semiconductors such as gallium nitride (GaN) and aluminum nitride (AlN) with nonpolar growth direction, [11-20] or [1-100], is promising material in high-efficiency light emitting device. [21] However, large size wafers growth of III-N is difficult. Recently, Horita et al. reported the growth of high crystal quality AlN on 4H-SiC(11-20) substrates by using an atomically flat SiC surface and optimized V/III ratio.[22] Nevertheless AlN structure is naturally wurtzite, they grown 4H-AlN on 4H-SiC(11-20) with low density of stacking fault and threading dislocation. They confirmed grown AlN structure by high-resolution transmission electron microscopy (HRTEM). However, interface atomic structure had never been observed directly in detail in spite of the importance for the device application. It is essential to characterize interface atomic structure for understanding the origin of device characteristic.

1.5 Purpose

The purpose of this study is the development of atomic and electronic structure analysis method for the hetero interface of semiconductor devices for an improvement of growth condition to make ideal hetero interface structure.

Chapter 2

Principle of Experiment

2.1 X-ray photoelectron spectroscopy (XPS)

When the photon is incident on an material, the material absorbs the energy of the photon(hν) and emit the electron. If the energy of the photon is higher than the binding energy of the electron, the electron can escape from the material as a photoelectron. This phenomena is called "photoemissive effect" Photoelectrons escape from the material with losing energy of work function. The binding energy (E_B)is obtained by

$$E_B = h\nu - E_k - \Phi \tag{2.1}$$

Where E_k is the photoelectron kinetic energy and the Φ is the work function of the material. The binding energy changes according to its chemical configuration. Thus, we can obtain the atom bonding information.

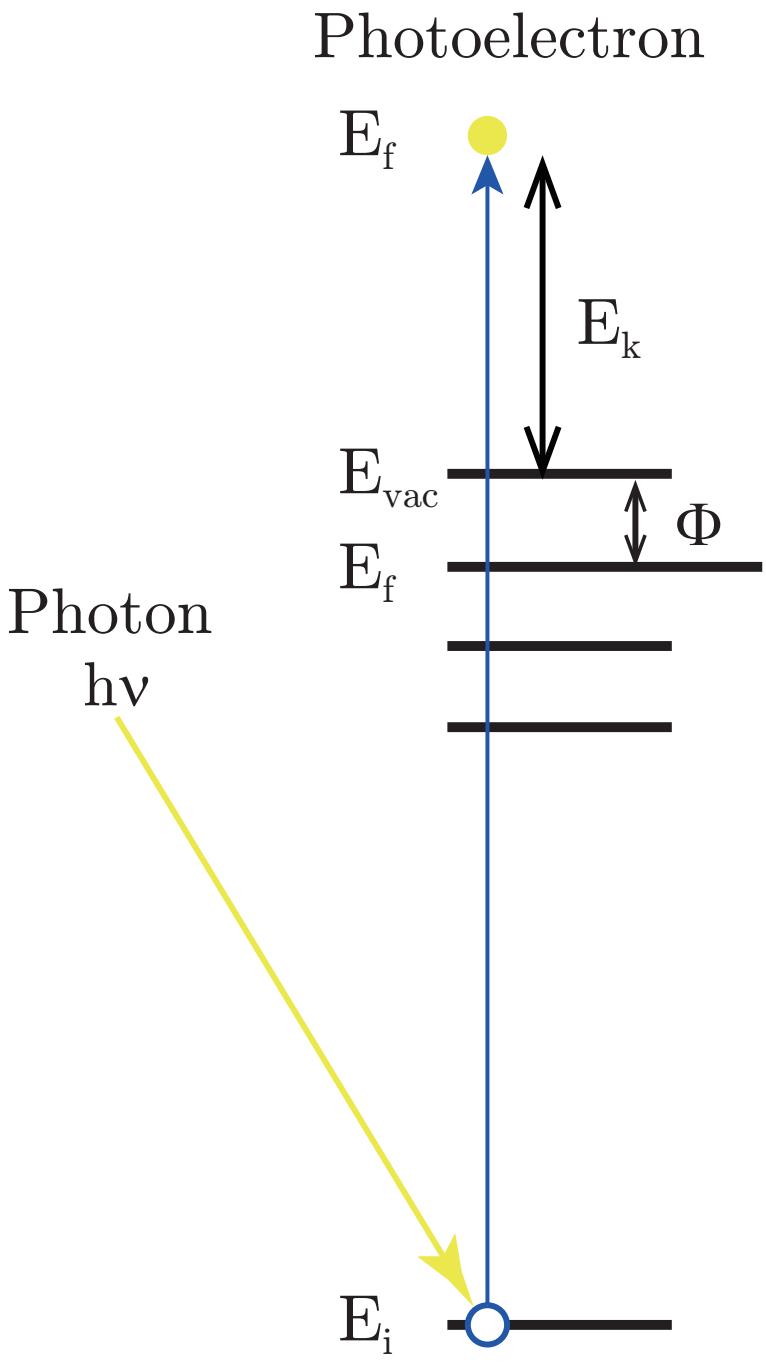

Fig. 2.1: The schematic diagram of photoelecron emissoin process

2.2 X-ray photoelectron diffraction (PED)

When the emitted photoelectron is scattered by surrounding atoms, scattered wave make large scattering amplitude at the surrounding atom direction. In addition associated wave of direct wave and scattered wave make zero order diffraction peak at the surrounding atom direction. These two peaks make large peak in photoelectron intensity angular distribution. The peak is called "Forward focusing peak". The Photoelectron diffraction can describe as shown below

$$\mid \Psi \mid^2 = \mid \psi_0 + \psi_s \mid^2 \; = \mid \psi_0 \mid^2 + \psi_0\psi_s^* + \psi_s\psi_0^* + \mid \psi_s \mid^2 \tag{2.2}$$

Where the ψ_0 is wave function of emitted electron and the ψ_s is wave function of scattered electron by surrounding atom. The Ψ is associated wave of these two. The first, second and third order diffraction peaks make diffraction rings.

$$kR(1 - \cos\theta_n) = 2\pi n + \delta n = 1, 2, 3... \tag{2.3}$$

We can estimate inter-atomic distance from this formula.

When, the circularly polarized light is used for photoelectron diffraction experiment,the FFP directions from the emitter atom to the scatterer atoms in the PIADs obtained by different helicity lights rotate around the incident light axis.

The rotation angle $\Delta\phi$ is well described by Daimon's formula:[31]

$$\Delta\phi = \tan^{-1} \frac{m}{kR \sin^2 \theta_{\text{out}}}, \tag{2.4}$$

where m and k are the magnetic quantum number and the wave number of photoelectron, respectively. R is the interatomic distance between the emitter and scatterer atoms, θ_{out} is the angle between the incident photon direction and the outgoing direction of the emitted photoelectrons. In general, the effective magnetic quantum number m^* considering the contribution of the transition probability from different m_{core} initial states at a particular angle is used [31]. In the case of O 1s excitation, m^* is 1.

$$| \Psi |^2 = | \psi_0 + \psi_s |^2$$
$$= | \psi_0 |^2 + \psi_0 \psi_s^* + \psi_s \psi_0^* + | \psi_s |^2$$

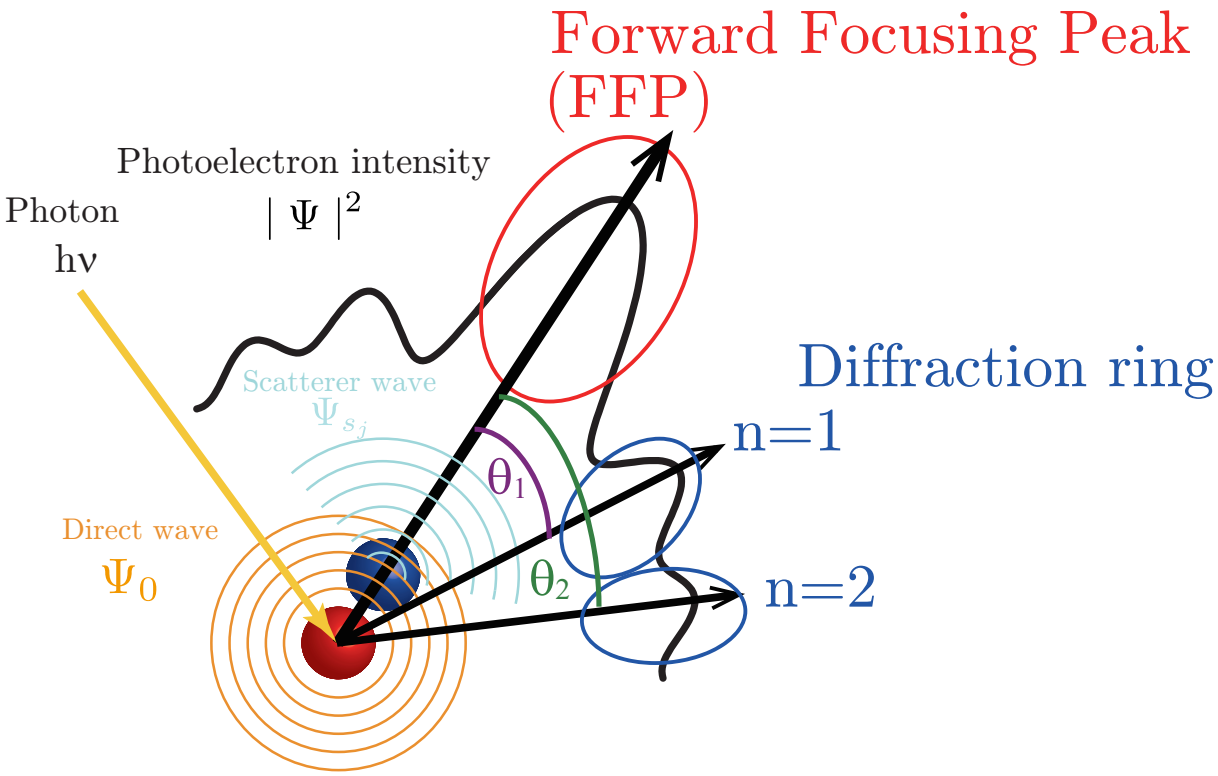

Fig. 2.2: The schematic diagram of photoelectron diffraction

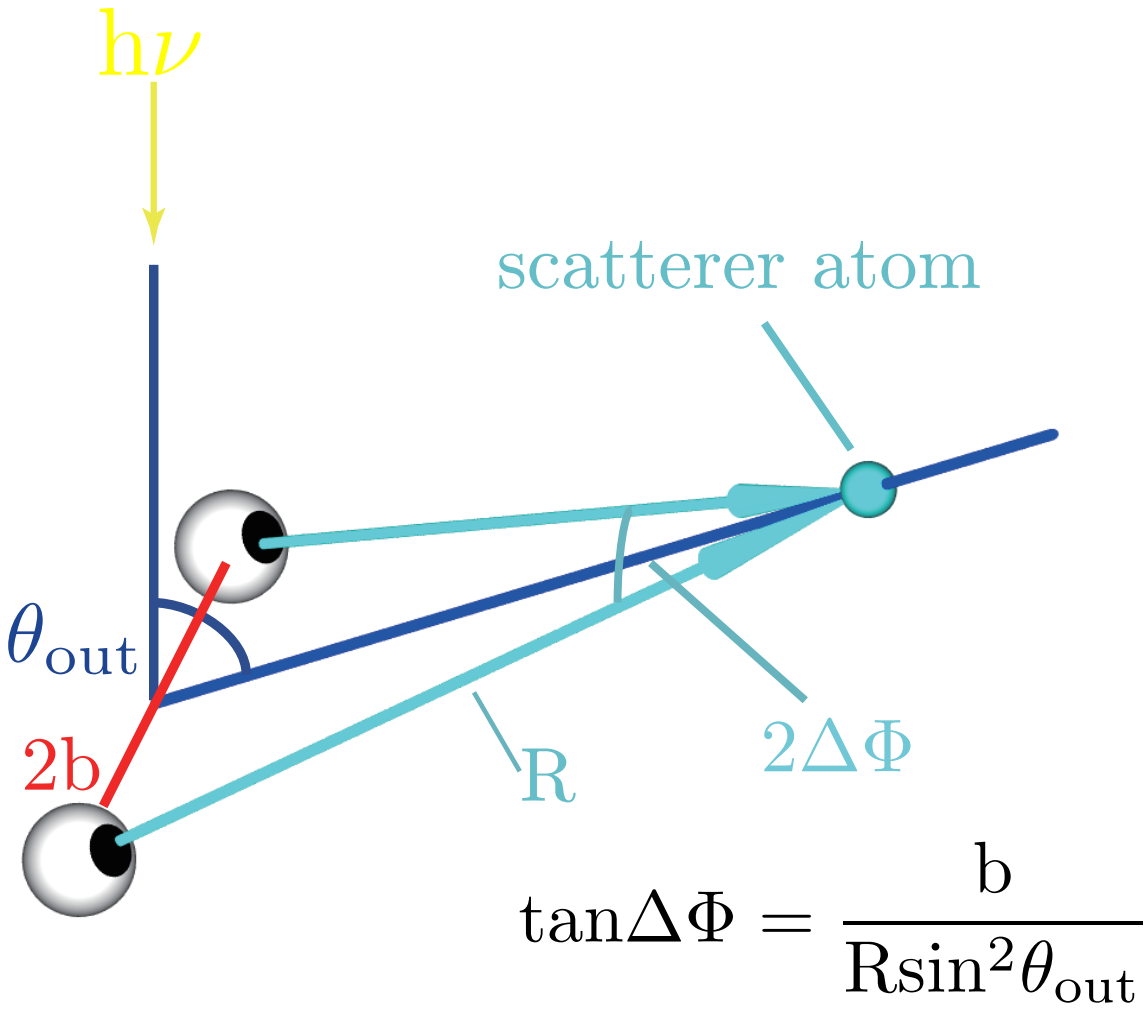

Fig. 2.3: The principle of the FFP parallatic angle shift by circularly polarized light.

2.3 X-ray Auger electron spectroscopy (AES)

The Auger electron is a kind of secondary electron escaped by the process as shown below

1. the photoelectron emitted by photon
2. the electron which grand state is higher than escaped photoelectron grand state fall to core hole
3. the Auger electron can escape from atom by the energy from photoelectron in 2

We can analyze what energy of photon was absorbed from the kinetic energy of Auger electron. However, chemical shift analysis is difficult due to much many state related in Auger process.

2.4 X-ray absorption spectroscopy (XAS)

The x-ray which have the energy hν emitted the electron in the atom. The electron absorb the energy of x-ray and escape from the atom. The crossection of x-ray absorption was obtained by Fermi's golden rule.

$$W \propto \frac{4\pi^2}{h} \mid M_{if} \mid^2 \delta(E_f - E_i - h\nu) = \frac{4\pi^2}{h} \mid < \psi_f \mid r \mid \psi_i \mid^2 \delta(E_f - E_i - h\nu) \quad (2.5)$$

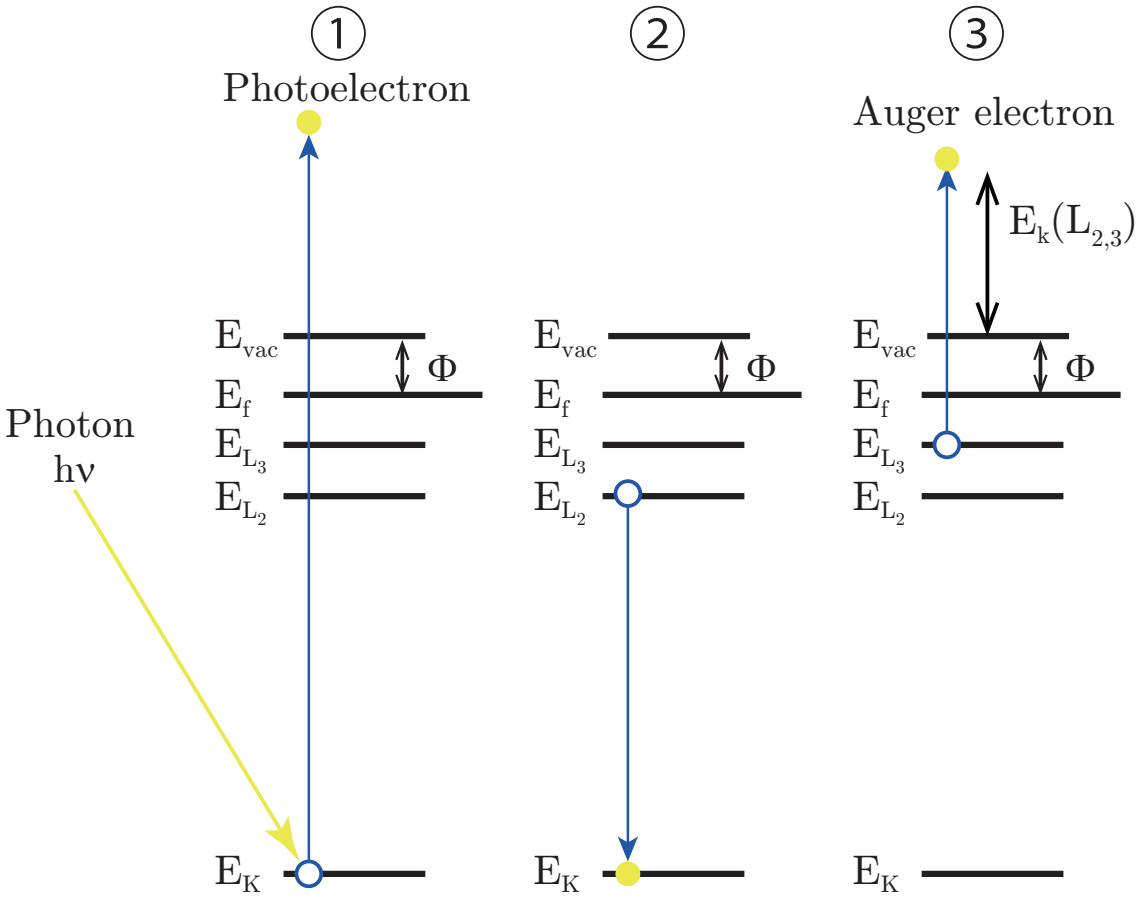

Fig. 2.4: The schematic picture of Auger electron emission process

where the E_i is a grand state energy of electron. The E_f is a final state energy of photoelectron. The ψ_i and the ψ_f is the grand and the final state wave function , respectively. The M_{ij} is an electron dipole moment.

2.5 Principle of Display-type spherical mirror analyzer (DIANA)

In this study I used Display type spherical mirror analyzer(DIANA) as photoelectron diffraction spectroscopy measurement equipment.

When the x-ray incident to a material, the photoelectron escapes from the material. The photoelectron's orbit is an ellipse in DIANA owing to the spherical electric field. The higher energy photoelectron than detection kinetic energy is absorbed at low pass filter. The lower energy photoelectron than detection kinetic energy is rejected by high pass filters after focus point of photoelectron. Then, the photoelectron which have detection kinetic energy is projected to fluorescent screen with keeping emission angle of photoelectron. The acceptance angle of the analyzer is $\pm 60^\circ$.

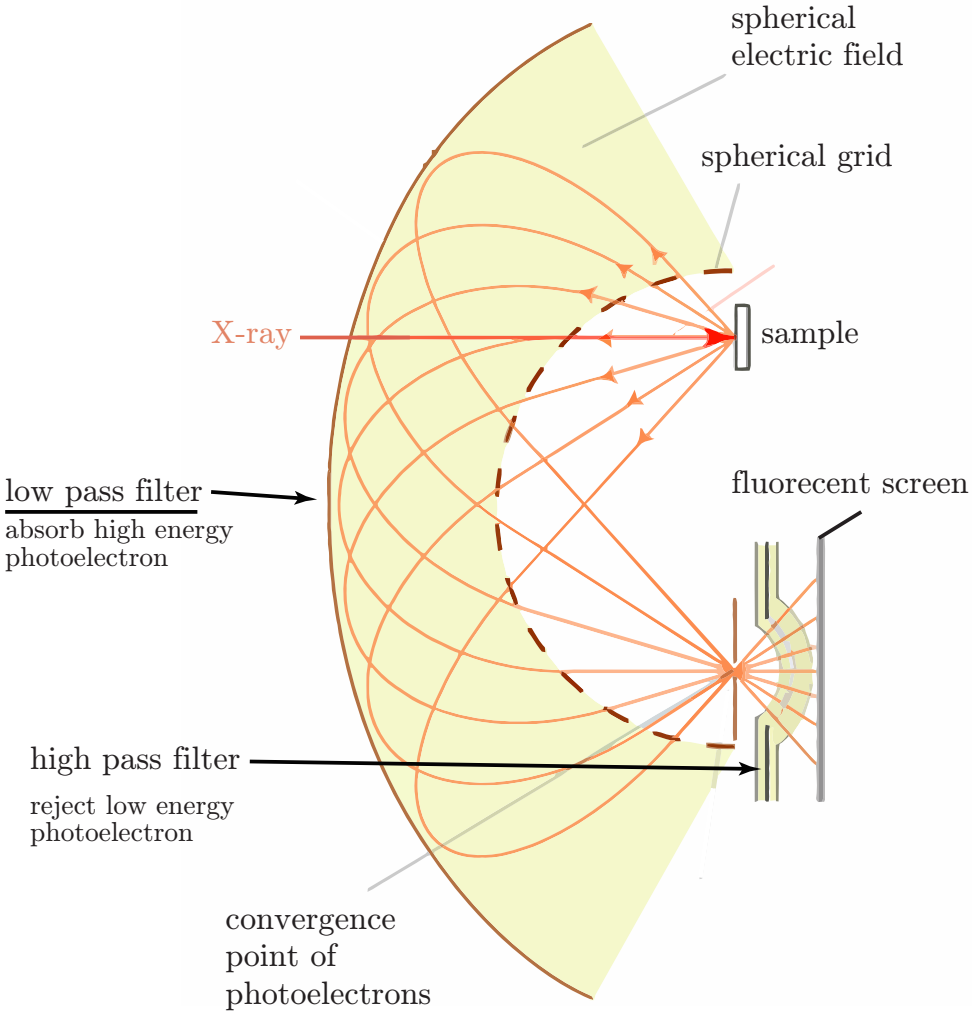

Fig. 2.5: Principle of DIANA

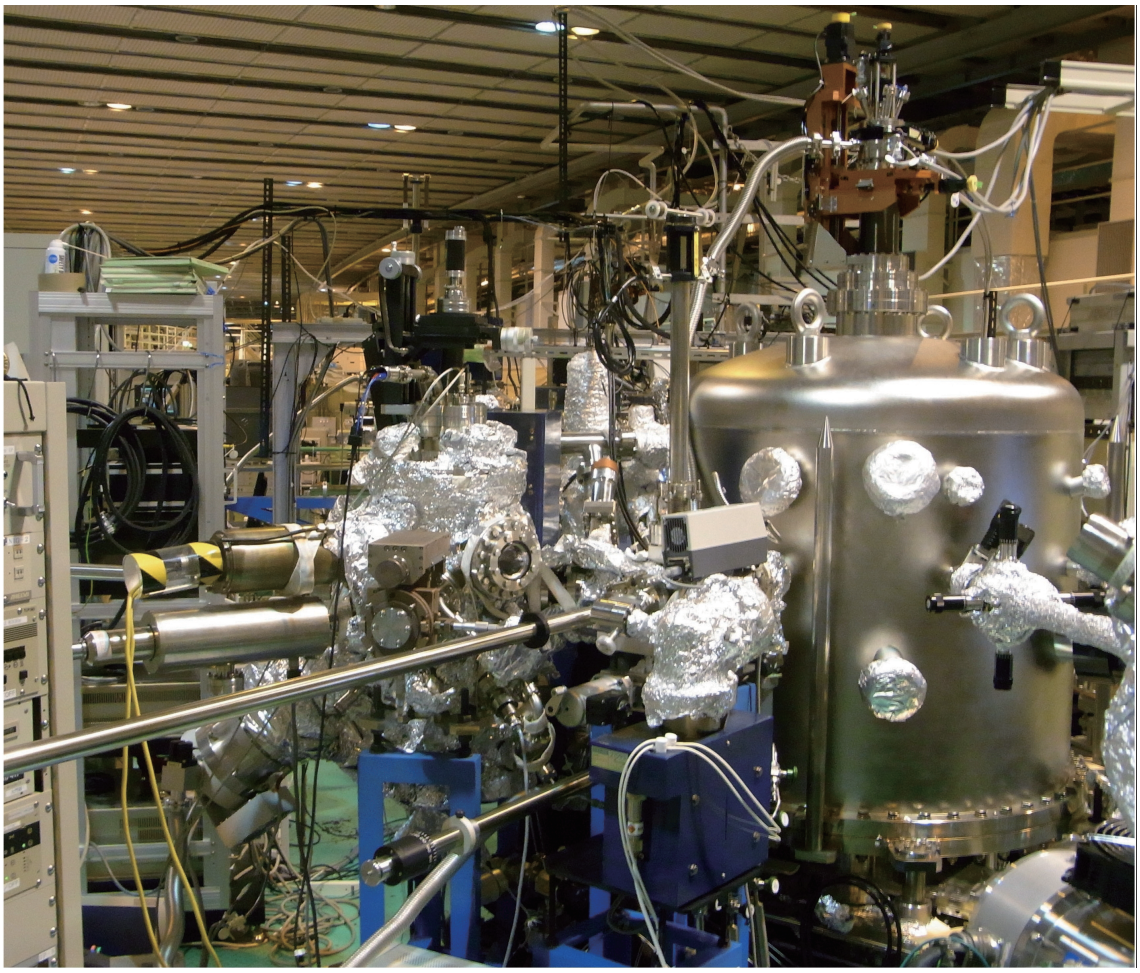

Fig. 2.6: The photograph of DIANA chamber at BL25SU SPring-8 Japan

Chapter 3

Investigation of the interface and thin film of the silicon oxynitride thin film on SiC

The film and interface structures of silicon oxynitride (SiON) thin film grown on the SiC(0001) surface were investigated by photoelectron diffraction. Forward focusing peaks (FFPs) corresponding to the directions from photoelectron emitter atom to surrounding atoms appeared in the photoelectron intensity angular distribution (PIAD). By comparing N 1s PIAD with those of Si 2p and C 1s, I confirmed that the nitrogen atoms at SiON/SiC interface substitute carbon atoms at the stacking fault sites. Two kinds of oxygen atom sites exist in the previously proposed model [17]. FFP corresponding to Si-O-Si perpendicular bonds was observed in the O 1s PIAD, while diffraction rings were observed in KLL Auger electron intensity angular distribution (AIAD), which were attributed to the diffraction patterns from outermost oxygen sites. Furthermore, O K-edge X-ray absorption spectra combined with AIAD were analyzed. Electronic structure specific to each oxygen

atom site was successfully separated.

Next, I have analyzed the post-nitridized oxide film on the SiC(0001) surface by using depth-resolved x-ray photoelectron and absorption spectroscopy. I have investigated the defect states in the oxynitride thin film. The SiC substrate with native oxide film was annealed at 700°C in UHV condition and exposed to 5000 L (1×10^{-6} Torr $\times$ 5000 sec) of NO gas. I measured the 2D x-ray photoelectron spectra (XPS) and x-ray absorption near edge structure (XANES) using Display-type spherical mirror analyzer (DIANA). From the emission angle dependence of XPS, we determined the oxide film thickness to be 1.0 nm. Furthermore, I analyzed the series of emission angle dependent XANES and separated into the contribution from the surface and interface regions. I propose that 399-eV peak state in the surface spectrum is attributed to π^* orbital of NO and the defect states at interface are quenched by N atoms. By using this method, the characterization of the electronic structure of oxide film becomes possible.

3.1 Experimental condition

The experiments were performed at the circularly polarized soft-X-ray beamline BL25SU of SPring-8, Japan.[23] The epitaxial SiON thin film was grown on the 6H-SiC(0001) surface with an off angle of 4° towards the $[1\bar{1}00]$ direction.[12] The sample was introduced into an ultra-high vacuum chamber and no further sample

surface treatment was applied. All experiments were performed at room temperature.

PIADs from the sample were measured using a two-dimensional display-type spherical mirror analyzer (DIANA). [24, 25, 26] The acceptance angle of the analyzer was $\pm 60^\circ$. Circularly polarized light was incident along the direction 45° off the surface normal in the O 1s PIAD measurement, while normal incident geometry was used for all the other measurements. In the case of normal incidence, the emission angle (θ) dependence from $45 \pm 60^\circ$ relative to the surface normal was measured simultaneously. By scanning the sample azimuth over 360°, 2π-steradian PIAD data were collected. A set of 2π steradian PIADs excited by σ_+ and σ_- helicity lights was measured by switching the path of storage ring electrons in twin helical undulators at 0.1 Hz.[27] Angle-resolved constant-final-state (CFS) mode photoelectron spectra and X-ray absorption spectra were obtained by varying photon energy at a fixed kinetic energy.

The density of states and molecular orbital calculations were performed using the first-principles program SCAT, a discrete varitional Xα molecular orbital method,[28] to interpret the experimental results. The molecular orbital result was explained by the Mulliken method. The final values of electrical densities were calculated until the result converges to the initial value assumed before the numerical basis function was obtained.

3.2 Atomic structure analysis of SiON thin film by PED

Figure 3.1 shows angle-resolved CFS-mode photoelectron spectra at a kinetic energy of 600 eV. The substrate components (Si 2p and C 1s) and the SiON thin film specific components (N 1s and O 1s) were observed. The peak intensity ratio of N 1s to O 1s was smaller at the surface sensitive grazing angle condition. This result indicates that the oxide layer was grown on the nitride layer.

I have measured the 2π-steradian Si 2p and C1s PIADs with a photoelectron kinetic energy at 600 eV using photon energy of 708 and 889 eV, respectively. In a bulk crystal, pairs of mirrored local atomic sites with respect to the $\{1\bar{1}00\}$ plane exist and the chemical environments surrounding each site are equivalent. However, all the measured patterns showed a threefold symmetry owing to the anisotropic step bunching along the $[11\bar{2}0]$ direction resulting a preferential appearance of terraces with one type of local atomic site.[29] Taking the finite inelastic mean free path of photoelectrons into account, photoelectron patterns for one kind of Si and C atom sites were successfully derived.[12] Figure 3.2(a) shows C 1s PAID from one kind of atomic sites near interface. The surface normal direction at the center of PIAD matches the sample rotation axis. The raw data were normalized by their polar angle intensity profile obtained by averaging their azimuthal intensity variations. The inhomogeneity of the detector can be removed

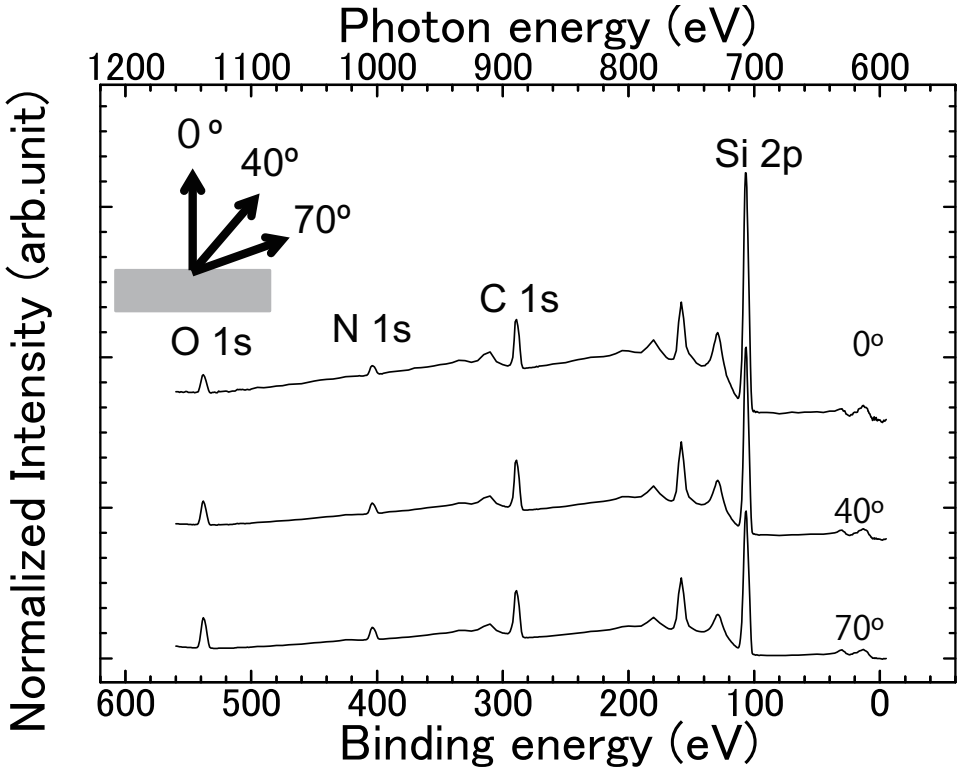

Fig. 3.1: The angle-resolved constant final state mode photoelectron spectra of SiON thin film on 6H-SiC(0001). The photoelectron kinetic energy was fixed at 600 eV and photon energy was varied. The intensity was normalized by C 1s peaks. The signal-to-background ratio at N 1s was 0.07.

in this normalization process. The pattern at the normal direction disappears by this procedure.

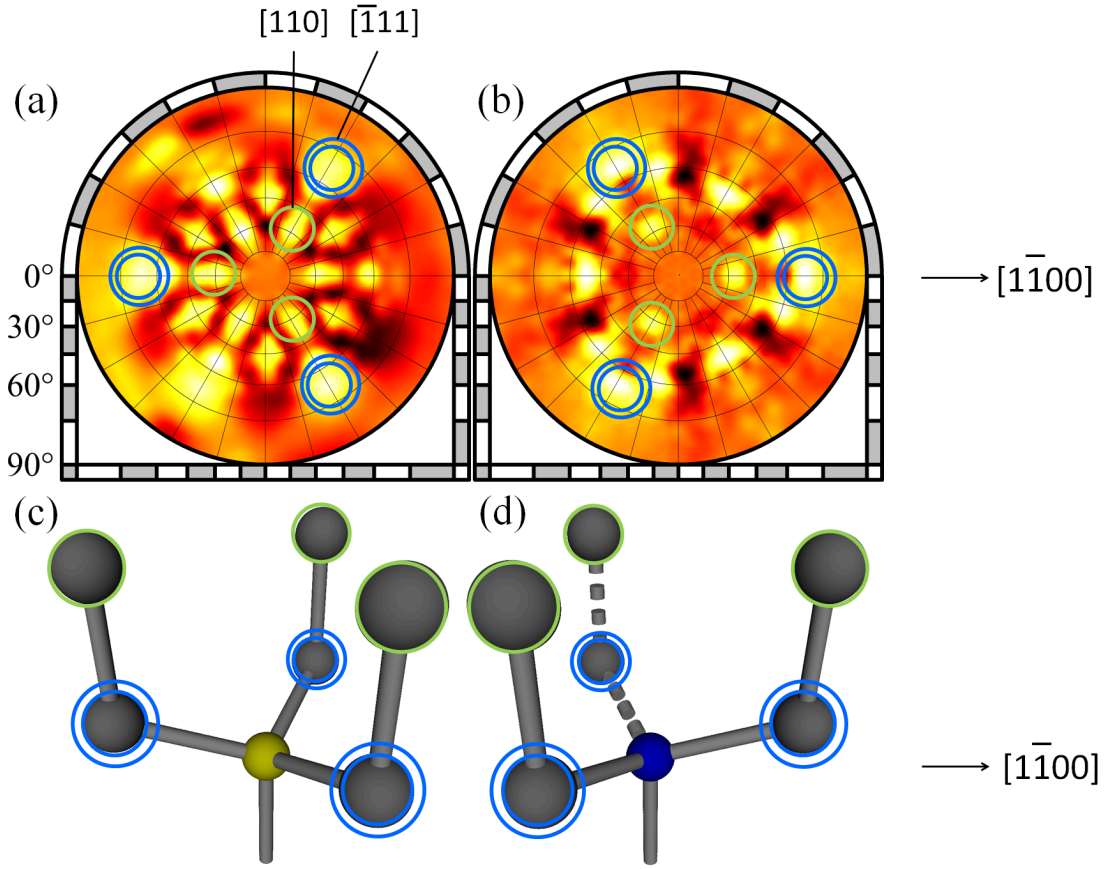

Fig. 3.2: (a) topmost unit site C 1s PIAD[12] and (b) N 1s PIAD patterns. The FFPs corresponding to the first and second nearest neighbor atoms were indicated by the blue double circles and green circles, respectively. The local atomic structure models expected from C 1s and N 1s PIAD patterns are shown in (c) and (d), respectively.

N 1s PIAD (Fig.3.2(b)) with a photoelectron kinetic energy of 600 eV was measured using excitation photon energy of 1003 eV. However, the signal-to-

background ratio at N 1s was very small because of energy-loss electron background as shown in Fig.3.1. I measured the background PIAD, which has same kinetic energy and exciting photon energy 20-eV lower than that of N 1s. Primary N 1s PIAD pattern was obtained by subtracting this background pattern in order to remove undesired energy-loss effects.[30]

The N 1s PIAD pattern was compared with the Si 2p (Fig.3(b) in Ref.[12]) and the C 1s (Fig.3.2(a)) PIAD patterns. Note that the C 1s PIAD pattern for topmost SiC unit site have a similar feature as the N 1s PIAD pattern, but mirror symmetric with respect to the $\{1\bar{1}00\}$ plane. Three FFPs corresponding to the first nearest neighbor atoms indicated by blue double circles as well as three FFPs corresponding to the second nearest neighbor atoms indicated by green circles were observed in the $\{11\bar{1}\}$ and $\{011\}$ directions in the the C 1s PIAD, respectively.[12] In contrast, FFPs corresponding to the first and second nearest neighbor atoms in N 1s PIAD were observed in the directions mirror symmetric with respect to the $\{1\bar{1}00\}$ plane. As shown in Fig.3.3(c), this indicates the substitution of carbon atoms with nitrogen atoms at the stacking fault site. Although, a nitrogen atom form three Si-N bonds with two Si atoms above and one Si atom directly beneath, there are three nitrogen atoms in one unit cell at the interface resulting three-fold symmetric PIAD pattern. These observations much agree with the suggested atomic structure model by Shirasawa *et al.*[17]

Figure 3.3(a) shows the circular dichroism in O 1s photoelectron angular distributions (CDAD) from the Si_2O_5 layer. Photoelectron kinetic energy was 600 eV and excitation photon energy was 1138 eV. Red cross indicates the direction of incident circularly polarized light. The white and black pattern at the center is the result of FFP rotational shift. Here I show that this feature is well reproduced by photoelectron diffraction simulation. I used a multiple scattering simulation code, TMSP, developed by one of our authors (T. Matsushita).[32] O 1s PIADs excited by σ_+ and σ_- helicity circularly polarized light from Si-O-Si linear cluster with Si-O bond length of 0.163 nm were simulated and CDAD pattern was obtained.

Note that the observed CDAD pattern is exactly reproduced in the simulated pattern shown in Fig. 3(b). Oxygen photoelectron emitter atom corresponds to atom indicated as O2 in the third layer as shown in Fig. 3(c). FFP circular dichroism pattern at the [0001] direction correspond to the Si atom indicated as Si1 in the second layer. Green circles in Fig. 2(b) correspond to O2 atoms seen from the N atom at interface. Therefore, I succeed in a direct observation of the 180° Si-O-Si bond.

Figure 3.4(a) shows O KLL 2π-steradian AIAD with a kinetic energy of photoelectron at 504 eV and excitation photon energy of 540 eV. The measured O KLL AIAD agrees well with the simulated pattern shown in Fig.3.4(b) for SiON structure model shown in Fig.3.4(c). Six FFP patterns indicated by black dots

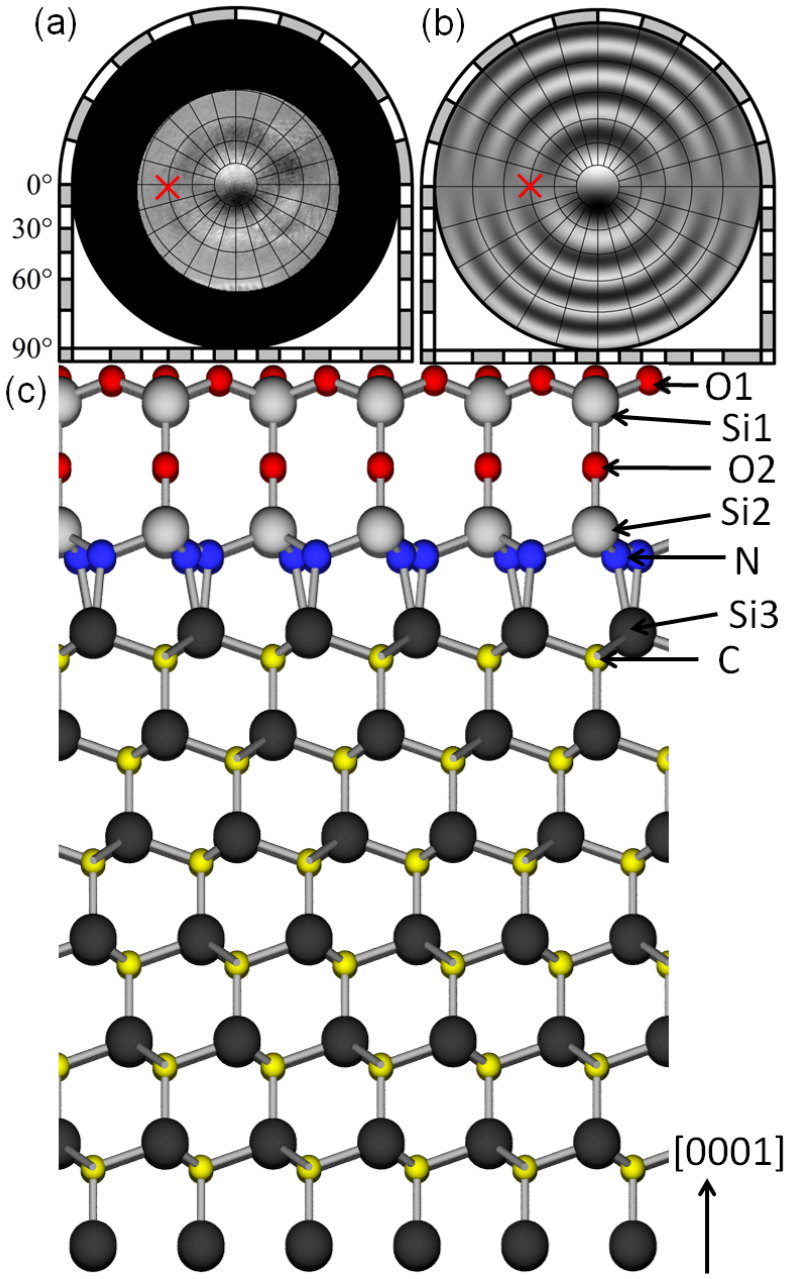

Fig. 3.3: (a) O 1s circular dichroism angular distribution pattern and (b) the corresponding multiple scattering simulation pattern. The red cross shows the direction of incident light. (c)The side view of atomic structure model of SiON thin film on 6H-SiC(0001) by Shirasawa *et al.*[19]

at the polar angle of 36° correspond to O1 atoms at the first layer seen from O2 atom at the third layer. The other diffraction patterns can be explained by the overlaps of diffraction rings indicated as R1, R2, and R3. These diffraction rings correspond to the in-plane O-O atom scatterings of r1, r2, and r3 indicated in Fig. 4(c).

3.3 Site specific electronic structure analysis by depth-resolved XAS

Finally,I measured the O K-edge XAS at normal incidence and emission polar angle from -15° to 90°. Figure 3.5(a) shows emission angle dependent XAS at every 10° from 5° to 85°. In the previous work, the XAS data obtained by TEY and AEY detection modes did not show much difference[19]. On the other hand, I succeeded in detecting gradual change as function of emission polar angle as shown in Fig.3.5. The intensity variation was 2% at the photon energy of 538 eV and the energy position of absorption maximum around 540 eV was shifted by 0.2 eV. Since mean escape depth of Auger electron varies by emission angle, these spectral changes suggest the difference in the local electronic structure for the first and third layer oxygen atom sites.

Therefore I analyzed these emission-angle-resolved XAS data to obtain depth

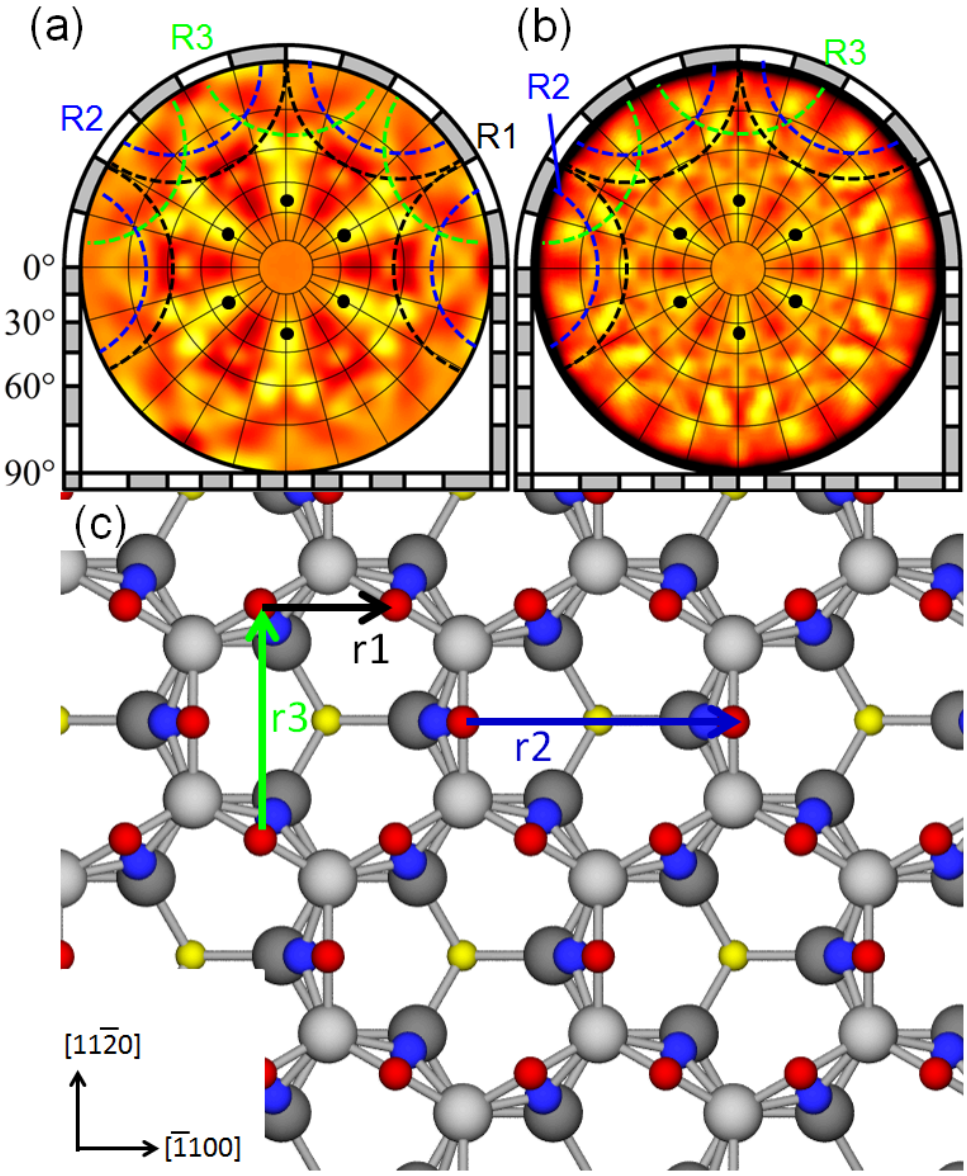

Fig. 3.4: (a) 2π-steradian O KLL Auger electron intensity angular distribution (AIAD) pattern and (b) the simulated result. There are five O atom sites, thus the AIAD from these sites were summed.

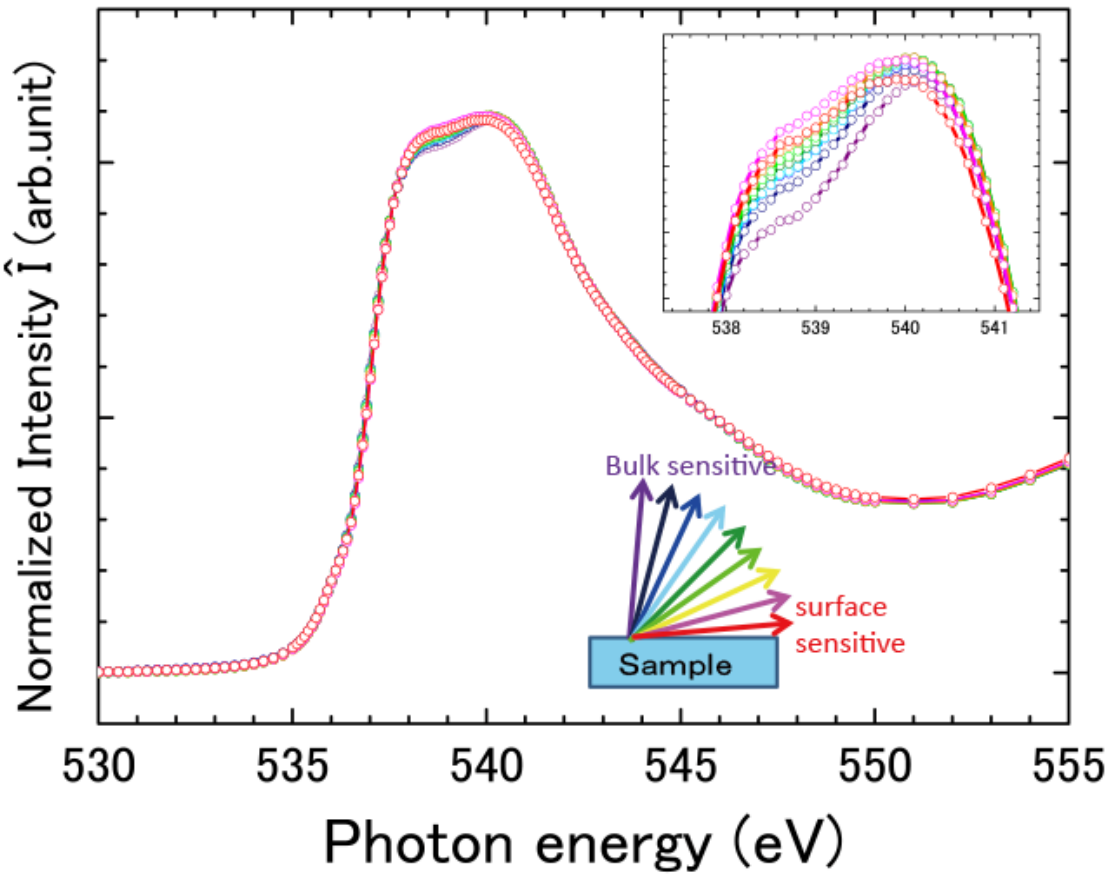

Fig. 3.5: The result of angle resolved Auger electron yield X-ray absorption spectrum.

dependent information. Measured intensity $\hat{I}_{\theta_x}$ for emission angle of θ_x are the sum of Auger electron intensity from the first and third layer O atoms and can be expressed as

$$\hat{I}_{\theta_0} = (3I_{1_{\rm st}} + 2AI_{3_{\rm rd}})/(3+2A) \tag{3.1}$$

$$\hat{I}_{\theta_1} = (3I_{1_{\rm st}} + 2BI_{3_{\rm rd}})/(3+2B) \tag{3.2}$$

$$A = \exp(-d/\lambda cos\theta_0) \tag{3.3}$$

$$B = \exp(-d/\lambda cos\theta_1) \tag{3.4}$$

where d is the depth of third layer oxygen atom site (0.215 nm) and λ is the Auger electron inelastic mean free path (1.79 nm). In order to separate spectra for the first and third layer O atom sites, $I_{1_{\rm st}}$ and $I_{3_{\rm rd}}$, respectively, I solved the following equation.

$$\begin{pmatrix} (3+2A)\hat{I}_{\theta_0} \\ (3+2B)\hat{I}_{\theta_1} \end{pmatrix} = \begin{pmatrix} 1 & A \\ 1 & B \end{pmatrix} \begin{pmatrix} 3I_{1_{\rm st}} \\ 2I_{3_{\rm rd}} \end{pmatrix} \tag{3.5}$$

Each layer spectrum obtained from this equation is normalized per atomic site. The separated XAS data for the first and third layer O atom sites are shown in Fig.3.6 as the black open circles and the red solid squares, respectively. The absorption edge locates at 536.2 eV (α) in both spectra. A broad peak appeared at 539.3 eV (peak γ) in the first layer spectrum, while two absorption peaks were observed at 538.1 (peak β) and 540.5 (peak δ) in the third layer spectrum. Note that the edge energy of both spectra were same. This result coincides with calculation

results. [19, 33, 34, 35]

Furthermore, I calculated electronic structure corresponding to the each peak as shown in Fig.3.6 by using SCAT code. SiH_3OSiH_3 clusters with bond angle of 144° and 180° were used to represent the first and third layer oxygen atom sites, respectively. The present normal incident geometry is sensitive to transition from O 1s to in-plane O 2p orbital. Here, molecular orbitals with considerable contribution of in-plane O 2p orbital are selected. The molecular orbital 3 expands in $\langle 11\bar{2}0 \rangle$ direction and is corresponding to γ peak. The molecular orbitals 2 and (4+5) expand in surface parallel direction around the third layer oxygen atom. Thus they are attributed to β and δ peaks.

Tanaka *et al.* calculated the density of states for α-quarts having 144° Si-O-Si bonds and β-cristobalite having 180° bonds.[36] Qualitatively, the present cluster calculation results agree with theirs. Since SiON thin film is a complex structure of α-quarts and β-cristobalite, crystal long range order does not exist. This seems to be the reason that the simulation using small cluster qualitatively explains site resolved XAS data.

Tridymite and cristobalite are the stable phase at the temperature range of 1000 $\sim$ 1700°C. SiON thin film were grown on the SiC substrate at the temperature of 1350°C. Thus it is natural to have 180° Si-O-Si bonds on such surface. However, distance between neighboring N atom is about 0.3 nm, which is too small for the

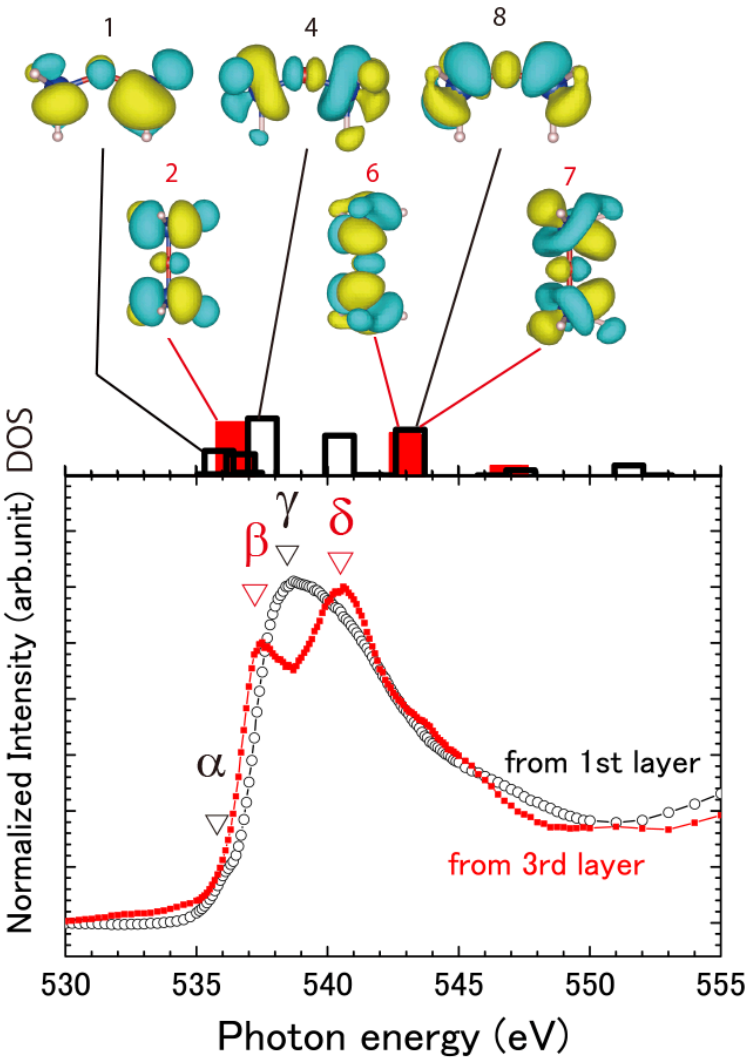

Fig. 3.6: The layer resolved X-ray absorption near edge structure spectrum with molecular orbitals calculated by DV-Xα. The normal incident circularly polarized light can excite the molecular orbital which direction is toward surface parallel. The red and black bar are O 2p density of state of Si-O-Si 144° and 180° atomic model. Each molecular orbital shown over the bar.

further tridymite crystal growth but just right distance for the 144° Si-O-Si bonds to terminate the surface. The resulting SiON thin film has no dangling bond and less strain. These are the origin of SiON thin film stability on this surface.

3.4 Electronic structure analysis of the amorphous silicon oxynitride thin film by depth resolved XPS

Firstly we investigate the detail of dispersion of N atoms in oxynitride thin film by angle-resolved CFS mode XPS. Figure 3.7 shows the results of N1s/O1s peak ratio in CFS mode XPS spectra at each detection angle from the SiON thin film and the NO post annealed sample. The SiON thin film has the nitrogen monolayer at the depth of 4.35 $\AA$ from the surface. The silicon oxide layer which is 3.75 $\AA$ thickness is on the silicon nitride layer. Considering decay of photoelectron intensity from the oxynitride film, the N1s/O1s peak ratio can be obtained by the formula as following

$$\frac{I_N}{I_O} = \frac{I_N^0}{I_O^0}\frac{X_N^0}{X_O^0}\frac{\lambda_N}{\lambda_O}\frac{\exp(-\frac{d_N}{\lambda_N \cos\phi}) - exp(-\frac{d_O}{\lambda_N \cos\phi})}{\exp(-\frac{d_O}{\lambda_O \cos\phi}) - 1} \tag{3.6}$$

Where I_Z is the peak intensity of the photoelectron excited from an inner shell in an element Z and I_Z^0 is the photoionization cross section of an inner shell in an element Z. X_Z is the concentration of an element Z in the SiON thin film. λ_N and λ_O are the inelastic mean free path of photoelectrons in the SiN layer and SiO layer, respectively. The calculated N1s/O1s CFS mode XPS peak ratio much agree with the experimental data in the range from 0° to 60°. The mean free path at the grazing angle becomes large because of the elastic scattering of photoelectrons in

the thin film. Thus, the calculated values do not agree with the experimental data at the grazing angle. Comparing the previous NO post annealed sample's data with the SiON thin film's data, these results indicate that nitrogen atoms widely diffused in oxynitride film of NO post annealed sample.

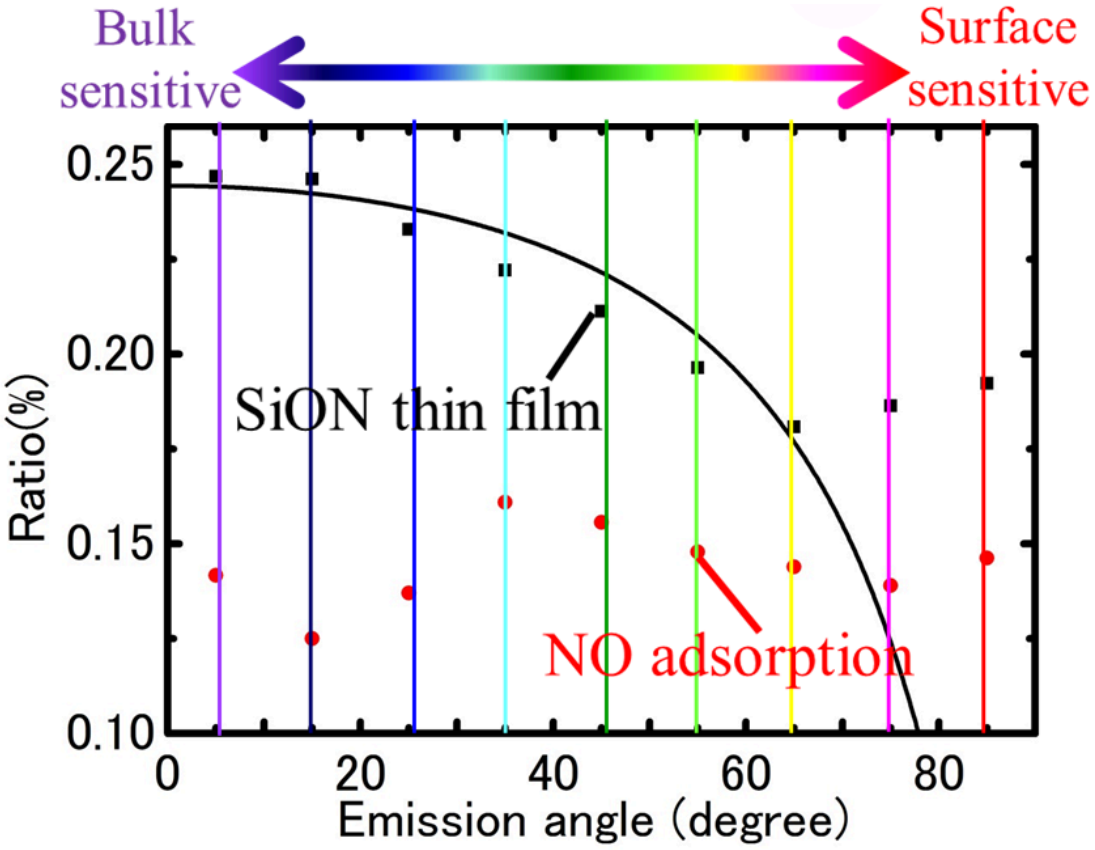

Fig. 3.7: The results of angle resolved N1s/O1s CFS-XPS of the SiON thin film and NO post annealed sample.

Figure 3.8 is the results of 2D-CFS-mode XPS spectra at a photoelectron kinetic energy of 600 eV. There are three N 1s peaks at the different emission angle

range. The probing depth of each detection angle d_θ can be obtained by

$$d_\theta = \lambda \cos\theta \tag{3.7}$$

The peak appeared at 398-eV is bulk sensitive because the emission angles from 40° to 85° where the probing depth is $\sim$ 1.3 nm. The peak appeared at 400-eV is surface sensitive because the emission angles range is from 75° to 90° where the probing depth is $\sim$ 0.4 nm. The weak peak appeared at 3973V is the emission angles from 65° to 90° where the probing depth is $\sim$ 0.7 nm. These peaks at 397, 398 and 400 eV correspond to C-N-Si_2, Si_3N and O-N-Si_2, respectively to refer to table 3.12.

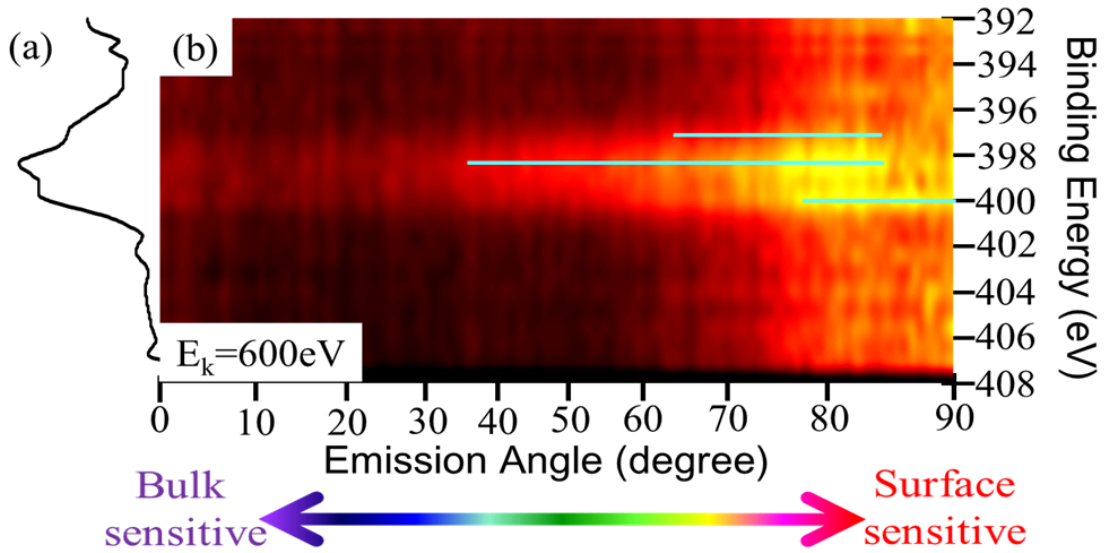

Fig. 3.8: (a) The spectra of CFS-mode N 1s photoelectron spectra integrated of all detection angles and (b)The result of 2D-CFS-mode photoelectron spectra at a photoelectron kinetic energy of 600 eV.

	Si_3N_4	SiO_xN_y	C≡ N	C-N	Si_3N	Si_2ON	SiO_2N	O_3N
Atomic Nitrogen passivation [37]	398.1	399						
Nitrogen in amorphous carbon[38]			398	400				
NO grown SiON film on SiC [39]					397.8			
SiO_xN_y thin film [19]					397.5	399.2	401.2	403.6

Table. 3.1: N 1s binding energy in various samples including N atom.

The SiON thin film has three nitrogen atoms per a unit cell. The square measure of unit cell is 41.14 Å= 0.4114 nm^2. The photoelectron mean free path is 1.6nm with a photoelectron kinetic energy of 600 eV in the case of the SiON thin film on SiC(0001). The probing depth is three times of that mean free path. Thus, there are three nitrogen atoms in the space of 1.974 nm^3 in the case of the SiON thin film. I calculated that the SiON thin film has 1.5 $\times$ 10^{21}atoms in the space of 1 cm^3. This is 0.0024 mol and 30 mg. Comparing with N 1s peak intensity in the case of the SiON thin film, I estimated that there are 1.0 $\times$ 10^{21}atoms in all NO post annealed oxynitride thin film. Furthermore, I estimated that the NO post annealed sample included $\times$ 10^{20} 3.9 $\times$ 10^{20} and 3.6 $\times$ 10^{20} N atoms as C-N-Si_2, Si_3N and O-N-Si_2 components from least square fitting by three nitrogen components, respectively.

3.5 Defect structure analysis of amorphous silicon oxynitride thin film by depth-resolved XAS

Figure 3.2 show the angle dependence of the N K edge XAS. The intensity variation was 15% at the photon energy of 399.6 eV and the energy position of the absorption maximum around 405.5 eV was not shifted. I assumed the existence of three

nitrogen components from the N 1s CFS results which I estimated in Chapter 3.4. Thus, each angle spectra were obtained by

$$\begin{aligned} I_{\theta_n}(E) = I_I(E) \int_0^{z_1} \exp(-\frac{z}{\lambda \cos\theta_n})dz \\ +I_{II}(E) \int_{z_1}^{z_2} \exp(-\frac{z}{\lambda \cos\theta_n})dz \\ +I_{III}(E) \int_{z_2}^{\infty} \exp(-\frac{z}{\lambda \cos\theta_n})dz \end{aligned} \tag{3.8}$$

where $I_{\theta_n}(E)$ is XANES spectrum at the emission angle θ_n. $I_m(E)$ is the XANES spectrum from the Region m (m=I,II,III). z_l is the depth of the boundary between the Region l and l+1 (l=I,II). $\exp(-\frac{z}{\lambda \cos\theta_n})$ is the decay function of the Auger electron.

There are three unknown spectra ($I_m(E)$). Formula **??** have two depth parameters z_1 and z_2 are in formula **??**. I decided the depth of z_1 and z_2 from N 1s peaks depth region at 397 eV and 400eV I estimated the oxide film thickness to be 1.0 nm from O 1s XPS result. N1s peaks at 397 eV and 398 eV indicate the boundary around 0.7∼1.3 nm. 5-step process of data analysis were performed to decide depth of z_1 and z_2, and choose the data analysis set from all emission angle data as shown below.

1. Select three experimental angle resolved spectra and, unknown z_1 and z_2
2. Solve simultaneous equations in three 3.8 formulas and obtain each unknown spectra $I_m(E)$

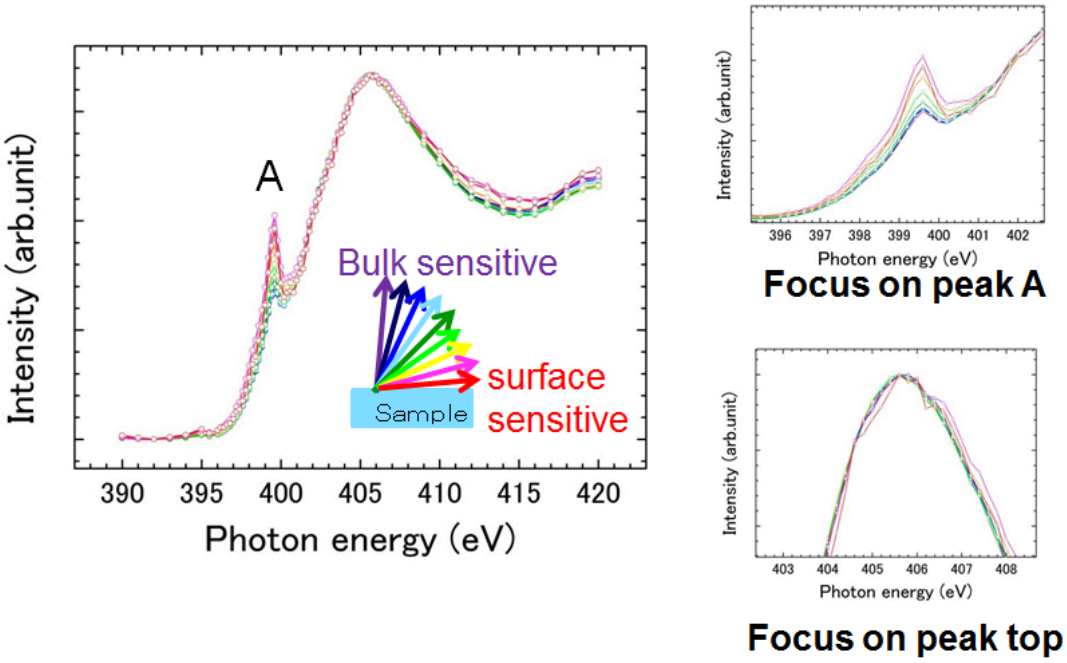

Fig. 3.9: (a) The result of angle resolved Auger electron yield X-ray absorption spectrum and,(b) and (c) enlarged drawing of each peak.

3. Substitute obtained $I_m(E)$ for formula 3.8 to get the spectra $I_{\theta_n}(E)$ from other emission angle θ_n by calculate equation

4. Compare experiment result each $I_{\theta_n}(E)$ with $I_{\theta_n}(E)$ calculated by least square fitting method

5. Repeat 1-4 process with changing parameters, finally I obtained the best parameter which result agree with all of angle resolved spectra

Performing these procedures, I obtained best three of θ_n are 5,65 and 85 degree and also, best the z_1 and z_2 set is the 0.3 nm and 1.0 nm as shown in Fig.3.3. 1.0 nm is the interface of oxide and bulk from XPS analysis. Region III includes the interface structure due to the native oxide roughness. Finally, I obtained the results of the depth resolved XANES as shown in Fig.3.4. I confirmed no defect states at the interface from Region III spectrum. However, I confirmed defect states in Region I and II, where are the oxide film and its surface.

Figure 3.12 and 3.13 are the estimation of conduction band minimum at Region I and Region II. The conduction band minimums are 399 ± 0.5 eV and 397.5 ± 1.0 eV at Region I and Region II, respectively. The defect state energies were 399.6 eV at both of Region. Thus, these defect states are not in middle of band gap but around conduction band minimum. These defect states which hold the free electrons become scatter for conduction electrons.

The incident angle dependence XAS spectra were shown in Fig.3.5. The peak A

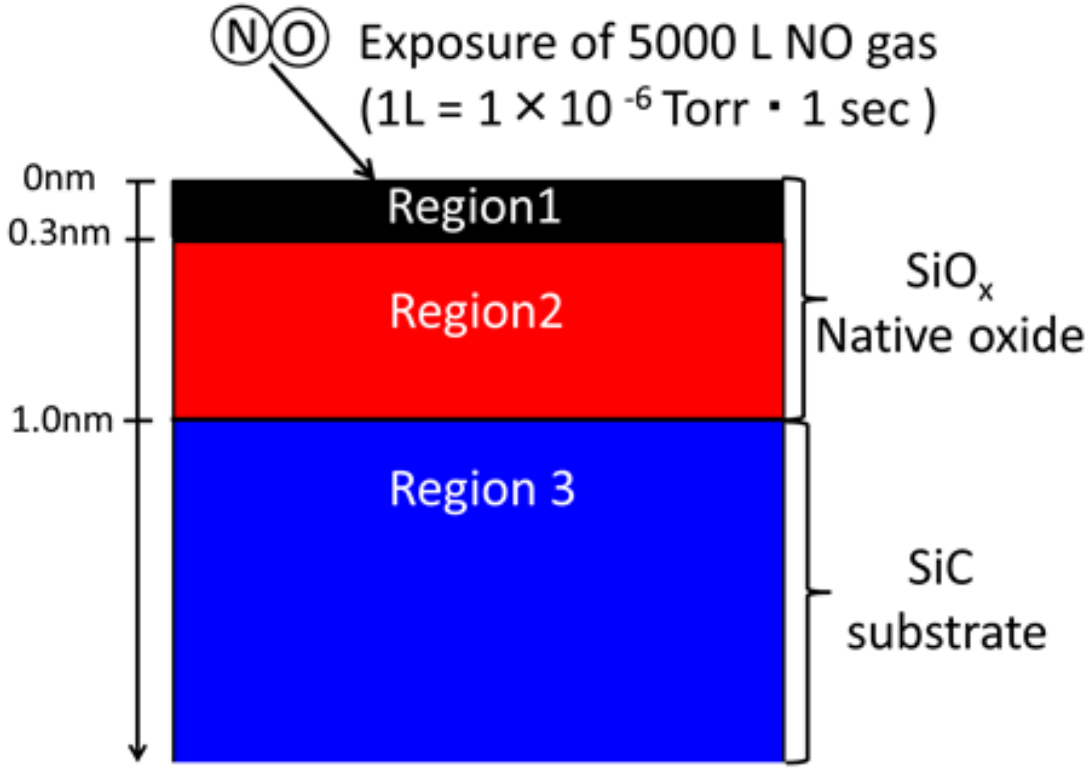

Fig. 3.10: The sample region obtained from the repeated procedures.

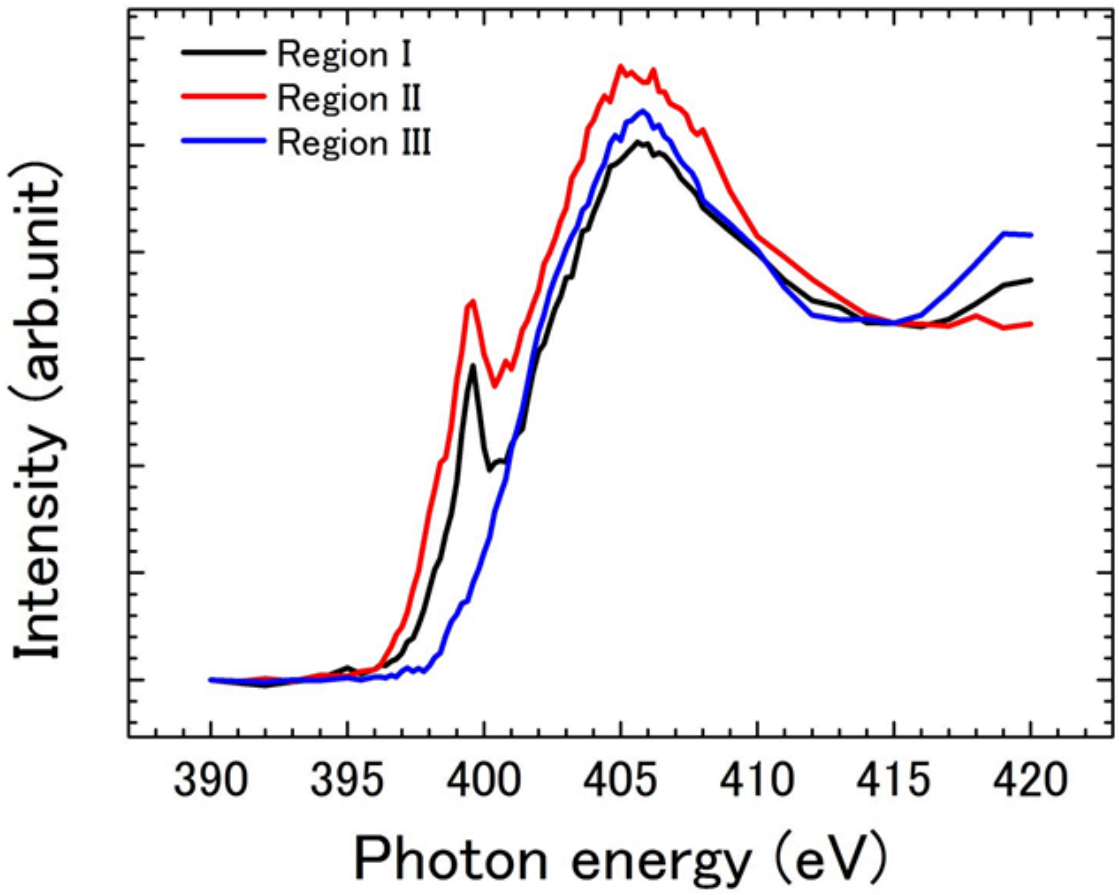

Fig. 3.11: The calculated result of layer resolved X-ray absorption near edge structure spectrum

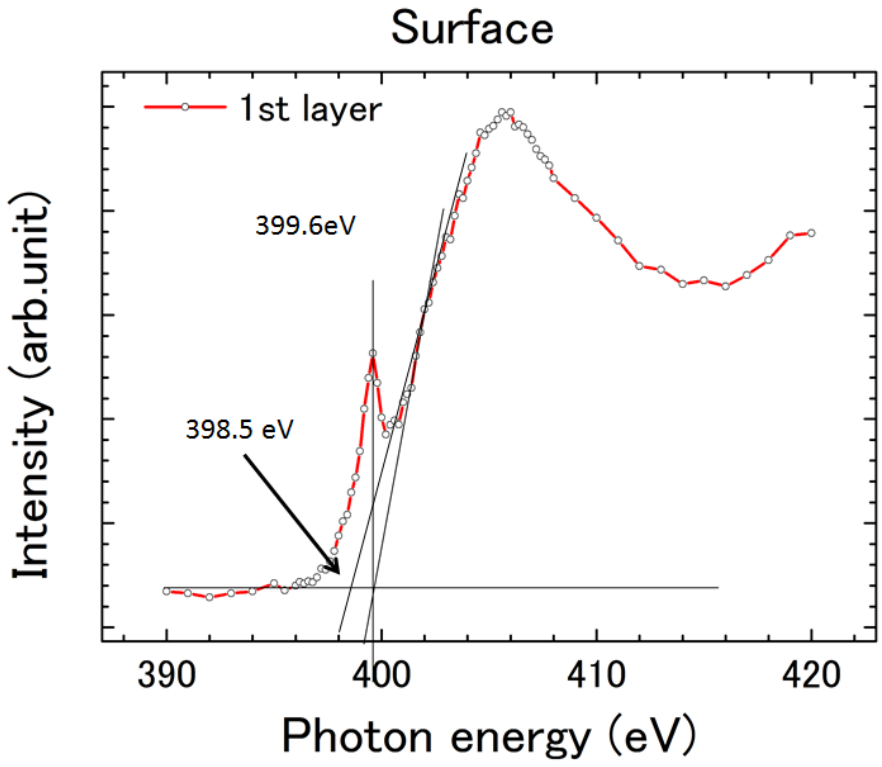

Fig. 3.12: The estimation of conduction band minimum at Region I

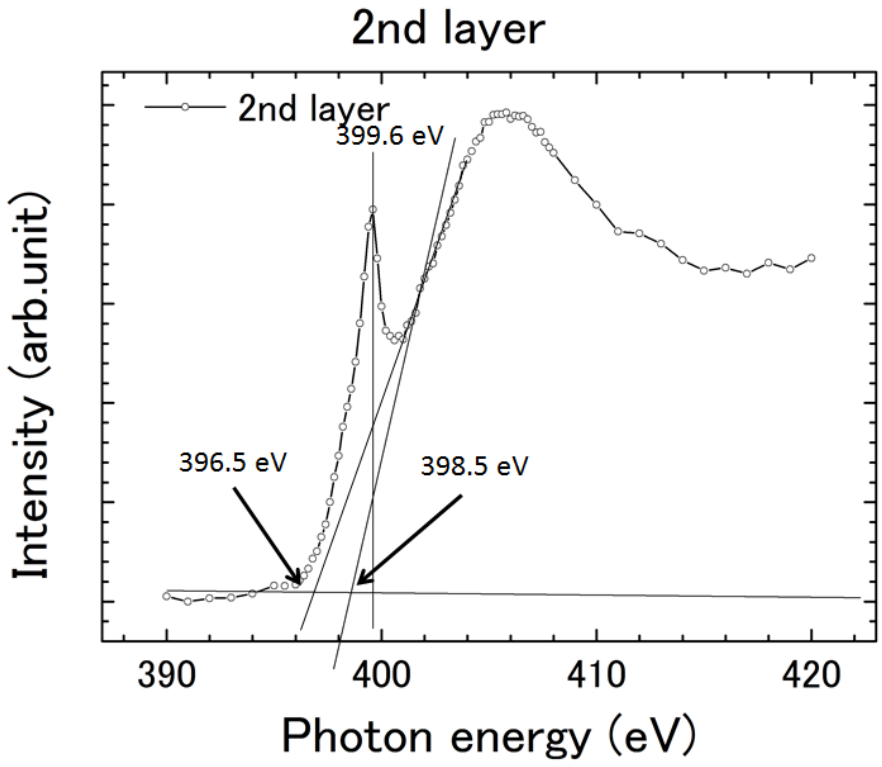

Fig. 3.13: The estimation of conduction band minimum at Region II

in these spectra were shown the incident angle dependence. I propose that peak A origin is N 1s$\rightarrow \pi^*$ transition at the surface. This results indicate that the residual NO molecules were detected around the surface.

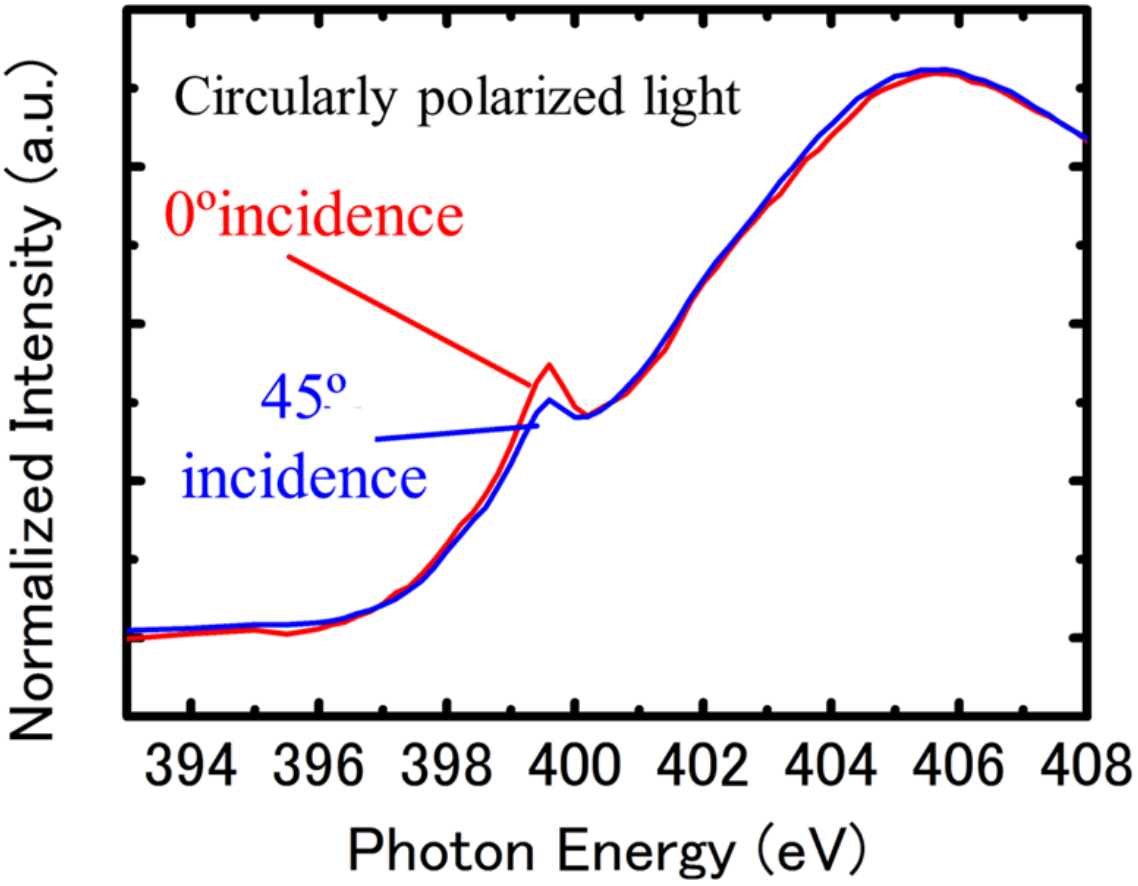

Fig. 3.14: The layer resolved X-ray absorption near edge structure spectrum

Chapter 4

Investigation of the interface and thin film of aluminum nitride on SiC

Group-III nitride semiconductors such as gallium nitride (GaN) and aluminum nitride (AlN) with nonpolar growth direction, $[11\bar{2}0]$ or $[1\bar{1}00]$, are promising material in high-efficiency light emitting devices. However, large size wafers growth of III-N is difficult. Recently, Horita et al. reported the growth of the high crystal quality AlN on 4H-SiC(11-20) substrates by using an atomically flat SiC surface and optimized V/III ratio. We measured angle resolved CFS mode XPS and XAS. I confirmed the chemical shift between surface and interface sensitive spectra in N 1s CFS mode XPS. I separate site specific PIAD pattern from two binding energy selective patterns from two site peak area ratio of CFS mode XPS. Finally, I succeeded in defect structure characterization of AlN/SiC(11-20) interface by two dimensional photoelectron diffraction spectroscopy.

4.1 Experimental condition

The experiments were performed at the circularly polarized soft-X-ray beamline BL25SU of SPring-8, Japan.[23] 7 ÅAlN grown on the 4H-SiC($11\bar{2}0$) surface in Kyoto University was transfered by high vacuum chamber to keep the thin film and the interface from oxidation. All experiments were performed at room temperature.

PIADs from the sample were measured using a two-dimensional display-type spherical mirror analyzer (DIANA). [24, 25, 26] The acceptance angle of the analyzer is $\pm 60°$. Circularly polarized light was incident along the normal direction from the surface parallel for all measurement. The emission angle (θ) dependence from $45 \pm 60°$ relative to the surface normal was measured simultaneously. By scanning the sample azimuth over 360°, 2π-steradian PIAD data were collected. A set of 2π steradian PIADs excited by σ_+ and σ_- helicity light was measured by switching the path of storage ring electrons in twin helical undulators at 0.1 Hz.[27] Angle-resolved constant-final-state (CFS) mode photoelectron spectra was obtained by varying photon energy with fixed kinetic energy.

4.2 Tin film and interface atomic structure analysis of 4H-AlN/4H-SiC by PED

Firstly, Al 2p and N 1s, which are the thin film specific components, PIAD patterns with a photoelectron kinetic energy of 600 eV were measured using excitation photon energies of 698eV and 1003 eV shown as Fig.4.1 (a) and (b), respectively. Si 2p and C 1s, which are the substrate specific components, PIAD patterns with a photoelectron kinetic energy of 600 eV was measured using excitation photon energies of 708eV and 889 eV shown as Fig.4.1 (c) and (d), respectively. The Al2p and the N 1s PIAD pattern have same structures with the Si 2p and the C 1s PIAD patterns, respectively. Therefor, the thin film AlN grown epitaxially on SiC($11\bar{2}0$) was confirmed. Next, I measured angle resolved Al 2p and N 1s CFS mode XPS as shown in Fig.4.2 (a) and (b). I confirmed the chemical shift between the surface and the interface sensitive spectra. The interface sensitive spectra can detect not only surface state but also interface state. Thus, the shift will be larger than the shift appeared in the spectra. N 1s site selective PIADs with a photoelectron kinetic energy of 600 eV was measured by using excitation photon energies of 1002.3 eV and 1003.3 eV. The sum and the difference patterns of these two patterns are shown in Fig.4.3 (a) and (b). The sum pattern is similar to N 1s PIAD from all sites(Fig.**??** (b)). However, the difference pattern shows new structure. This results indicate that the chemical shifted component has a

different atomic structure from the atomic structure in AlN thin film. Therefore, I expected that the interface atomic structure is different from the thin film AlN structure.

Table 4.1 is results of peak fitting for CFS mode XPS spectra by the SiN and the AlN components. I decide the binding energy of SiN component as 398 eV by the CFS mode XPS result of the SiN thin film on 4H-SiC($11\bar{2}0$). That sample was made by exposing NH_3 gas for a SiC($11\bar{2}0$) clean surface. I confirmed by photoelectron diffraction measurement that the SiN thin film was grown epitaxially on the SiC ($11\bar{2}0$) substrate. The AlN binding energy was 1.1 eV smaller than the SiN component. An XPS peak dose not formed Gaussian or Voigt function shape because of large retardation (1 eV) energy in measurement by using DIANA. The N 1s peak curve was obtained from the SiN CFS mode XPS measurements. The binding energy selective patterns are sum of two site selective patterns in each peak intensity ratio. I performed the least square fitting by these two components as shown in Table 4.1. I estimated that the ratio of two components in the binding energy selective pattern from Table 4.1. Thus, I can obtain site selective patterns from the follow matrix:

$$\begin{pmatrix} P_a & P_b \\ P_c & P_d \end{pmatrix} = \begin{pmatrix} P_{AlN} \\ P_{SiN} \end{pmatrix} \begin{pmatrix} P_{1002.3} \\ P_{1003.3} \end{pmatrix} \tag{4.1}$$

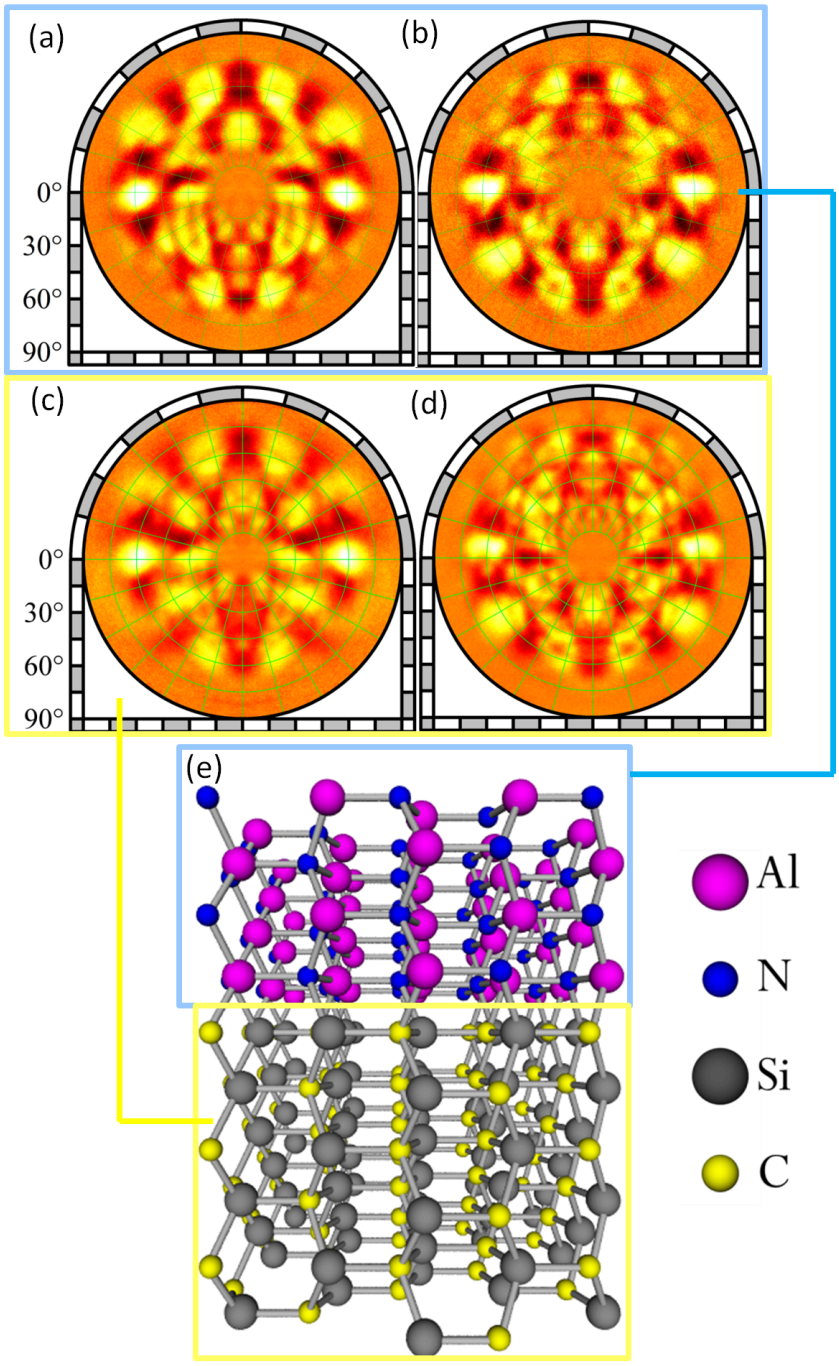

Fig. 4.1: The 2πsteradian PIADs from (a)Al 2p and(b) N 1s with a photoelectron kinetic energy at 600 eV using photon energy of 680 and 1002.8 eV, respectively. (c) and (d) are Si 2p and C 1s PIADs, which are from SiC(11$\bar{2}$0), with a photoelectron kinetic energy at 600 eV using photon energy of 708 and 889 eV, respectively. The ideal interface atomic structure model of AlN thin film on SiC(11$\bar{2}$0) is shown in (e)

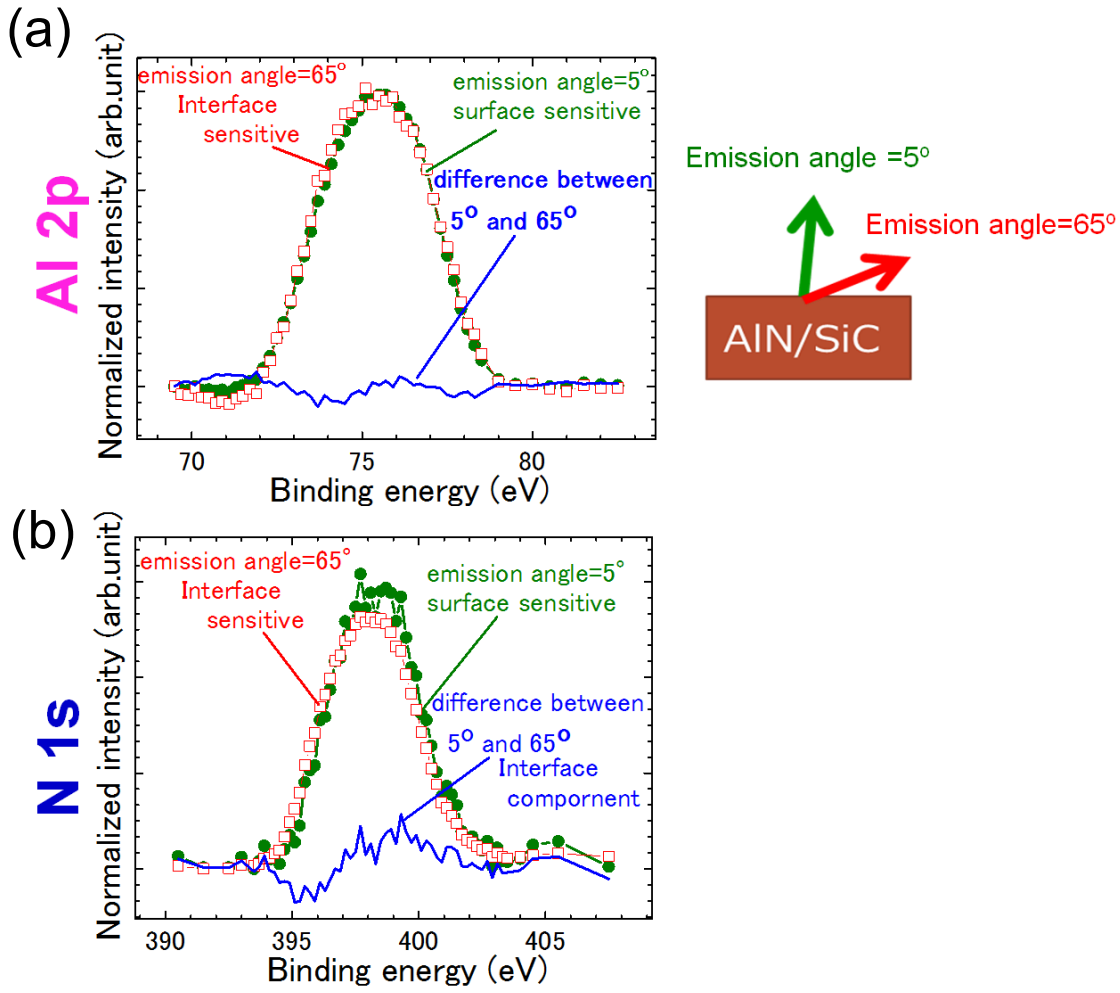

Fig. 4.2: The results of angle-resolved Al2p and N 1s CFS-mode XPS. The peak intensities were normalized by the intensity at peak top. Large emission angle (65°) spectrum is more surface sensitive than small emission angle (5°) due to the escape path becoming long with large emission angle. The interface and surface sensitive spectra indicated by open circle and square each other. Interface spectrum has deeper binding energy components than a surface spectrum.

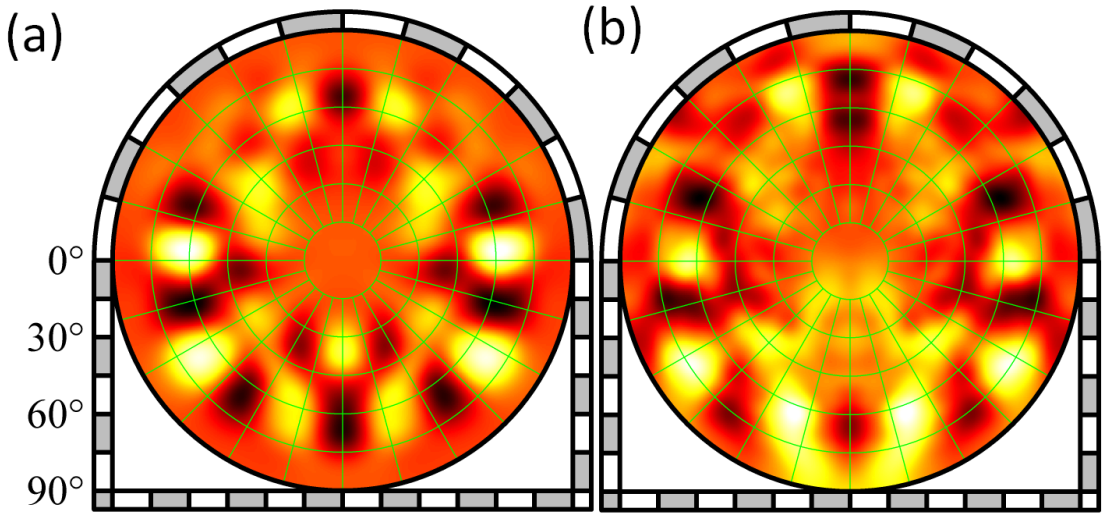

Fig. 4.3: (a) The sum of patterns measured with a photoelectron kinetic energy of 600 eV by using excitation photon energies of 1002.3 eV and 1003.3 eV. (b) The difference obtained by subtracting the patterns measured by using excitation photon energies of 1003.3 eV from 1002.3 eV

$$\begin{pmatrix} P_{AlN} \\ P_{SiN} \end{pmatrix} = \begin{pmatrix} P_a & P_b \\ P_c & P_d \end{pmatrix}^{-1} \begin{pmatrix} P_{1002.3} \\ P_{1003.3} \end{pmatrix} \tag{4.2}$$

where the $P_a \sim$ the P_d are the ratio of two components in 1002.3 eV and 1003.3 eV binding energy selective patterns. The P_{1002} and the P_{1003} are binding energy selective patterns measured by using excitation photon energy of 1002.3 eV and 1003.3 eV, respectively. The site-specific PIAD P_{AlN} and P_{SiN} are derived by solving an inverse matrix as shown in Fig.Fig3-2-4. The interface site selective pattern indicated that FFPs at around (θ, ϕ)=(60, 240) corresponding to third nearest neighbor atom appeared at higher polar angle position than a thin film site selective pattern. Other FFPs also appeared the same tendency. From these result, I considered the atomic structure around the interface specific sites shown in Fig.4.4 (c) $\sim$ (f). These structures localized in interface AlN layer. The nitrogen atom positions at the interface specific sites were shifted 0.2 Åbelow along [11$\bar{2}$0] direction comparing with the AlN thin film site because an Al-N bond length is 0.2 Ålonger than a Si-N bond length. I succeed in defect structure characterization of AlN/SiC(11$\bar{2}$0) interface by two dimensional photoelectron diffraction spectroscopy.

Finally, I try to make abrupt interface of AlN/SiC(11$\bar{2}$0). I expected that the origin of SiN layer is pre-exposed nitrogen gas due to making nitrogen radical process. Thus, I asked the sample producer that you deposited a small amount of

	AlN peak area ratio	SiN peak area ratio
5	0.659	0.341
15	0.760	0.240
25	0.769	0.231
35	0.772	0.228
45	0.823	0.177
55	0.849	0.151
65	0.801	0.199
75	0.758	0.242
85	0.779	0.221

Table. 4.1: The peak area ratios of AlN and SiN components at each emission angle in N 1s CFS mode XPS

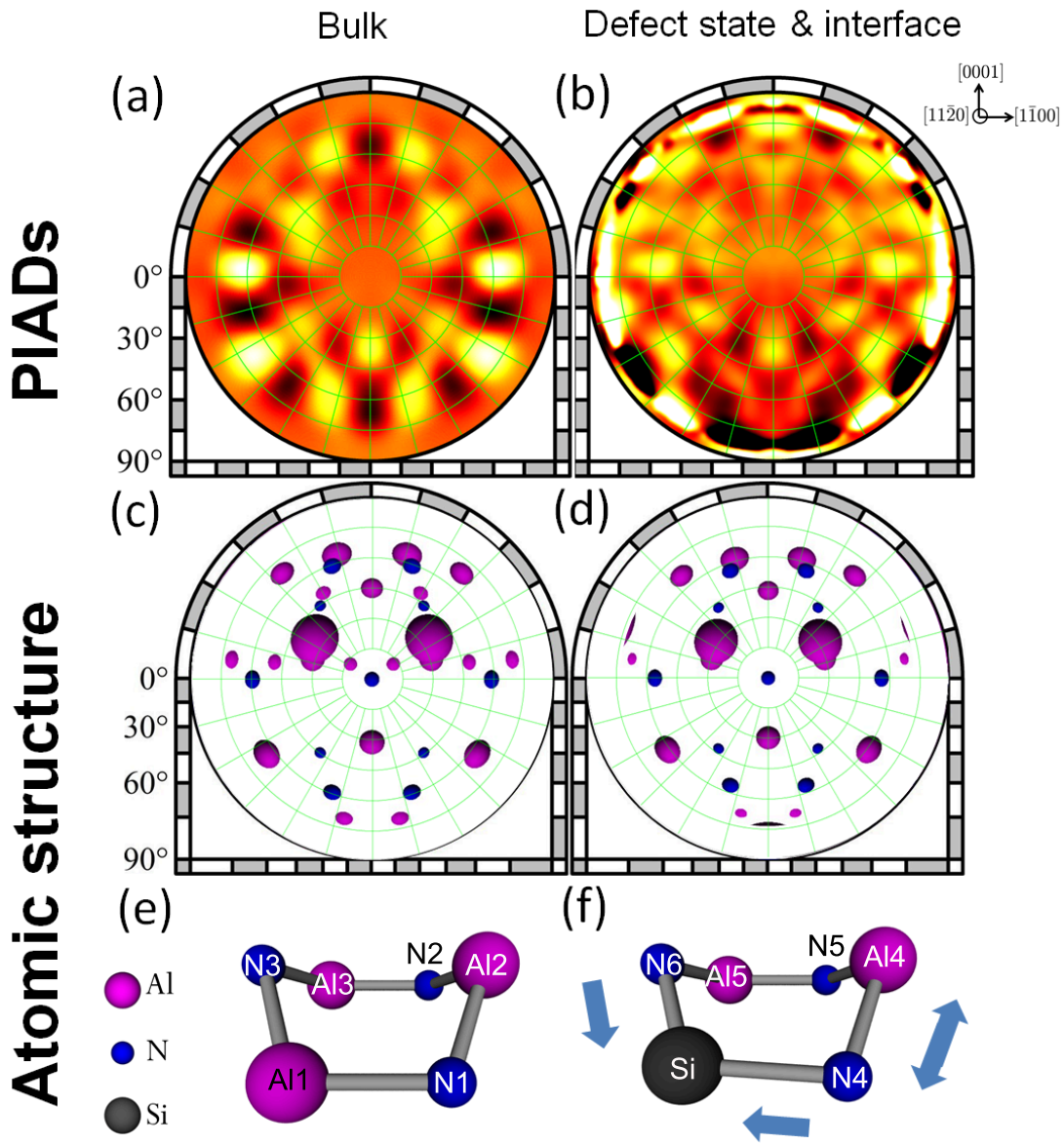

Fig. 4.4: (a) Thin film and (b) interface site selective PIADs and the PIADs calculated by formula (c) and (d). (e) and (f) are the atomic structures obtained from the patterns around the thin film and interface specific site. Around SiN defect N4 and N6 come close to Si atom because SiN bond is shorter than AlN in general. Thus Al4-N4 bond is longer than N6-Si bond. Thus, Al5 atom which is third nearest neighbor atom from viewing N4 atom is at higher polar angle than Al3 atom from N1 atom.

Al on SiC(11$\bar{2}$0) before nitrogen exposed. I measured angler resolved CFS mode XPS of this new sample. The results are shown in Fig. 4.5 (c) and (d). There are no angle dependence of peak energy. Thus, I succeeded in improving the hetero interface structure of the AlN/SiC(11$\bar{2}$0) interface.

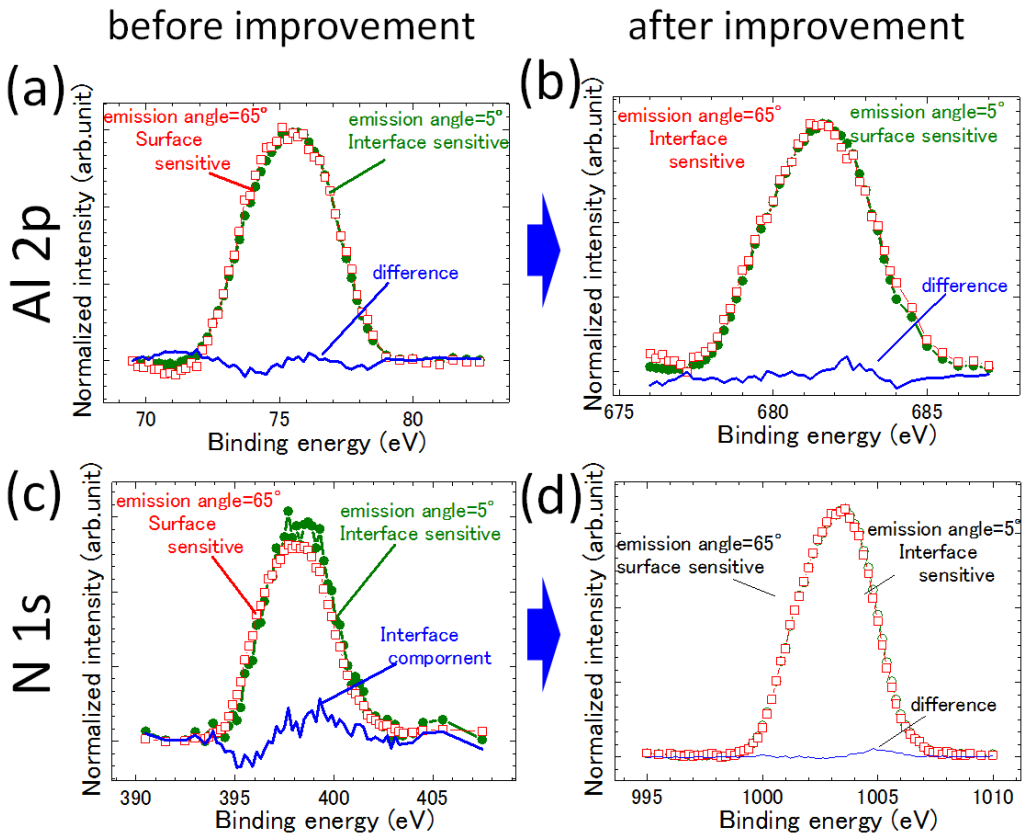

Fig. 4.5: The results of angle resolved Al2p and N1s CFS mode XPS spectra. (a) and (b) are Al2p and N1s CFS mode XPS spectra, respectively before improvement of the sample growth process. (c) and (d) are Al2p and N1s CFS mode XPS spectra respectively after improvement the sample growth process.

Chapter 5

Conclusion

In this study, I analyzed atomic and electronic structures of buried semiconductor device interfaces through element and site selective local atomic and electronic structure observations nondestructively by applying photoelectron diffraction spectroscopy method. As the result of atomic structure analysis I revealed

- the stacking fault at the semiconductor hetero junction interface
- the unexpected defect atomic structure at the semiconductor hetero junction interface

As the result of electronic structure analysis I obtained

- concentration of structural defects from the chemical shift of core level by angle-resolved XPS
- the energy of defect states in band diagram with high sensitivity by angle-resolved XAS

These results made that I revealed the effect of improving treatment for the semiconductor hetero junction interface as shown in the NO post annealed sample

analysis and the semiconductor hetero junction interface atomic structure analysis and its growth method as shown in AlN/SiC atomic structure analysis. As the result, I succeeded in developing the methods which can reveal interface atomic and electronic structure of the interface of buried semiconductor device and improve a crystal growth method.

Necessary equipment for this method.

In this study, I used synchrotron radiation at SPring-8 as x-ray source and DIANA as the analyzer. This methods use the Synchrotron radiation center, in this case especially SPring-8, in XAS measurements. When this methods use the conventional analyzer to measure the PIAD pattern, it takes not less than twenty forth times measurement time compare with using DIANA measurement. However, this methods can shorten it to limit the measurement region of PIAD pattern to required region for analysis.

Detection limit

This methods can detect defect atomic structures which concentration is one tenth in the sample from PIAD pattern. This methods can characterize the difference of not less than 2 degree bond angle difference or 0.2 Åatomic position shift between two atomic sites. However,we required the single crystal sample which size is lager than 0.03 mm^2 in the case of measurements at BL25SU in SPring-8. The detection limit of XPS measurements is 1.0×10^{21}atoms in a space of 1 cm^3. The

detection limit of XAS is ten times sensitive comparing with XPS measurements.

Advantage of this method

The big advantage of this method is detecting substitution atomic structure characterization nondestructively because this method is one of the few element specific atomic level characterization method. Furthermore, this methods are good at characterizing local atomic structure's symmetry and direction, and decide the sample front and back.

Acknowledgment

I would like to express my gratitude to Prof.Daimon who gives insightful comments and suggestions. I am particularly grateful for the assistance given by Prof. Matsui. I would like to thank Prof.Fuyuki Prof. Hosoito and,Prof. Hattori. They give a many advices in discussion. I would like to show my greatest appreciation to Dr. Matsushita. He give a many advices in experiments and analysis of its data. I have greatly benefited from Dr. Takeda. I appreciate grateful support with Dr. T. Nakamura and Dr. T. Muro. This research performed by Japan Synchrotron Radiation Research Institute (Proposal Nos. 2009A1753, 2009B1769, 2010A1468, 2012A1548, 2012B1487, 2013A1624, and 2013A1440). I want to thank other all laboratory members who make precious my five years with me. Finally, I have had the support and encouragement of my family, especially, my parents and my wife.

Bibliography

[1] C. S. Fadley and S. A.L. Bergstrom, Phys. Letters 35A, 375 (1971).

[2] A. Liebsch: Phys. Rev. Lett. **32** (1974) 1203.

[3] S. Kono, C. S. Fadley, N. F. T. Hall, and Z. Hussain: Phys. Rev. Lett. **41** (1978) 117.

[4] S. D. Kevan, R. F. Davis, D. H. Rosenblatt, J. G. Tobin, M. G. Mason, D. A. Shirley, C. H. Li, and S. Y. Tong Phys. Rev. Lett. **46**, (1981) 1629

[5] J. J. Barton, C. C. Bahr, Z. Hussain, S. W. Robey, J. G. Tobin, L. E. Klebanoff, and D. A. Shirley Phys. Rev. Lett. **51** (1983) 272

[6] D. A. Wesner, F. P. Coenen, and H. P. Bonzel Phys. Rev. Lett. **60**, (1988)1045

[7] S. A. Chambers and V. A. Loebs: Phys. Rev. Lett. **63** (1989) 640.

[8] S. Dreiner, M. Schurmann, C. Westphal, and H. Zacharias: Phys. Rev. Lett. **86** (2001) 4068.

[9] M. Schürmann, S. Dreiner, U. Berges, and C. Westphal: Phys. Rev. B **74**, (2006) 035309.

[10] F. Matsui, T. Matsushita, Y. Kato, M. Hashimoto, K. Inaji, F. Z. Guo, and H. Daimon: Phys. Rev. Lett. **100** (2008) 207201.

[11] F. Matsui, T. Matsushita, and H. Daimon: J. Electron Spectrosc. Relat. Phenom. **178-179** (2010) 221.

[12] F. Matsui, N. Nishikayama, N. Maejima, H. Matsui, K. Goto, M. Hashimoto, T. Hatayama, T. Matsushita, Y. Kato, S. Tanaka, and H. Daimon: J. Phys. Soc. Jpn. **80**, (2011) 013601.

[13] W. H. G.Pensl: *Silicon Carbide Recent Major Advances* (Springer, 2004).

[14] V. V. Afanas'ev, M. Bassler, G. Pensl, and M. Schulz: physica status solidi (a) **162** (1997) 321.

[15] J.Bernhardt, J. Schardt, U. Starke, and K. Heinz: Appl. Phys. Lett. **74** (1999) 1084.

[16] V. V. Afanas'ev, A. Stesmans, F. Ciobanu, G. Pensl, K. Y. Cheong, and S. Dimitrijev: Appl. Phys. Lett. **82** (2003) 568.

[17] T. Shirasawa, K. Hayashi, S. Mizuno, S. Tanaka, K. Nakatsuji, F. Komori, and H. Tochihara: Phys. Rev. Lett.**98**, (2007) 136105.

[18] T. Shirasawa, K. Sakamoto, T. Takahashi, and H. Tochihara: Surf. Sci. **605** (2011) 328.

[19] T. Shirasawa, K. Hayashi, H. Yoshida, S. Mizuno, S. Tanaka, T. Muro, Y. Tamenori, Y. Harada, T. Tokushima, Y. Horikawa, E. Kobayashi, T. Kinoshita, S. Shin, T. Takahashi, Y. Ando, K. Akagi, S. Tsuneyuki, and H. Tochihara: Phys. Rev. B **79** (2009) 241301.

[20] J. P. Chang, M. L. Green, V. M. Donnelly, R. L. Opila, J. Eng Jr., J. Sapjeta, P. J. Silverman, B. Weir, H. C. Lu, T. Gustafsson, and E. Garfunkel J. Appl .Phys. **87**, (2000) 4449.

[21] P.Waltereit, et.al. Nature (London) 406, 865 (2000).

[22] M. Horita, et.al. Appl. Phys. Lett. 89, 112117 (2006).

[23] Y. Saitoh, H. Kimura, Y. Suzuki, T. Nakatani, T. Matsushita, T. Muro, T. Miyahara, M. Fujisawa, K. Soda, S. Ueda, H. Harada, M. Kotsugi, A. Sekiyama, and S. Suga: Rev. Sci. Instrum. **71** (2000) 3254.

[24] H. Daimon: Rev. Sci. Instrum. **59** (1988) 545.

[25] H. Daimon and S. Ino: Rev. Sci. Instrum. **61** (1990) 57.

[26] M. Kotsugi, Y. Miyatake, K. Enomoto, K. Fukumoto, A. Kobayashi, T. Nakatani, Y. Saitoh, T. Matsushita, S. Imada, T. Furuhata, S. Suga, K. Soda, M. Jinno, T. Hirano, K. Hattori, and H. Daimon: Nucl. Instrum. Methods A **467-468** (2001) 1493.

[27] T. Muro, T. Nakamura, T. Matsushita, H. Kimura, T. Nakatani, T. Hirono, T. Kudo, K. Kobayashi, Y. Saitoh, M. Takeuchi, T. Hara, K. Shirasawa, and H. Kitamura: J. Electron Spectrosc. Relat. Phenom. **144-147** (2005) 1101.

[28] H. Adachi, M. Tsukada, and C. Satoko: J. Phys. Soc. Jpn., **45** (1978) 875.

[29] S. Nakamura, T. Kimoto, H. Matsunami, S. Tanaka, N. Teraguchi, and A. Suzuki: Appl. Phys. Lett. **76** (2000) 3412.

[30] F. Matsui, T. Matsushita, M. Hashimoto, K. Goto, N. Maejima, H. Matsui, Y. Kato, and H. Daimon: J. Phys. Soc. Jpn. **81**, (2012) 013601.

[31] H. Daimon: Phys. Rev. Lett. **86** (2001) 2034.

[32] T. Matsushita, F. Matsui, H. Daimon, and K. Hayashi: J. Electron Spectrosc. Relat. Phenom. **178-179** (2010) 195.

[33] P. Krüger, B. Baumeier, and J. Pollmann: Phys. Rev. B **77**, (2008) 085329.

[34] F. Devynck, Z. SljivanCanin, and A. Pasquarello: Appl. Phys. Lett. **91**, (2007) 061930.

[35] F. Devynck and A. Pasquarello: Surf. Sci. **602**, (2008) 2989.

[36] I. Tanaka, J. Kawai, and H. Adachi: Phys. Rev. B **52** (1995) 11733.

[37] J.W. Chai et al, Appl Phys Lett 92, 092119 (2008)

[38] B.Wai et al, J.Appl Phys 83, 2491 (1998)

[39] P. Jamet et al, Appl Phys Lett 79, 323 (2001)